Soil Dynamics and Earthquake Engineering 182 (2024) 108693

Contents lists available at ScienceDirect

Soil Dynamics and Earthquake Engineering

journal homepage: www.elsevier.com/locate/soildyn

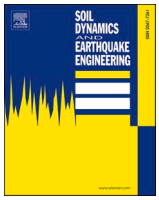

Experimental study of the dynamic tunnel response adjacent to a building

Zhengyao He *, Gopal S.P. Madabhushi

Schofield Centre, University of Cambridge, UK

A R T I C L E I N F O

Keywords:
Tunnel floatation
Liquefaction
Cut & cover tunnel
Soil-structure interaction (SSI)

A B S T R A C T

It is important to determine the dynamic behaviour of underground structures under cyclic loading for the seismic underground structural design. The dynamic response of such underground structures is further complicated when considering the interaction with surface buildings. This paper presents a series of dynamic centrifuge tests and 2D numerical modelling to investigate the dynamic response of a shallow cut-and-cover rectangular tunnel and the nearby building in the liquefiable sandy ground. Dynamic soil responses such as the wave propagation and excess pore pressure are successfully captured in both centrifuge testing and numerical modelling. Tunnel uplift, building settlement and soil deformation are determined by the particle image velocimetry (PIV) technique. Results show the existence of the nearby building can cause significant effects to the tunnel lateral movement and tunnel rotations. The tunnel floatation mechanism is also discussed with a simplified vertical force equation. In addition, the presence of the buried tunnel causes non-uniform settlement distribution along the building range. The comparison of the experimental, numerical building settlement with the analytical and empirical estimations proves the limitation of these methods in considering the building interaction with other structures.

1. Introduction

The development of underground tunnelling in urban areas has become more frequent, due to the growth of demand of space for utility, highway, and railway transportation in congested urban spaces. Shallow cut-and-cover tunnels are preferred in urban spaces as these are cheaper to build and technologically more straight forward to construct. Further, the cost of constructing a tunnel increases significantly with depth. However, these shallow tunnels can be close to the foundations of existing structures in an urban environment. During a strong earthquake, there can be a strong interaction between the tunnel and the foundations of nearby buildings. Recent seismic events, such as the 1995 Kobe earthquake in Japan [1], the 2008 Wenchuan earthquake in China [2], and the 2023 Turkey–Syria earthquake [3] indicated that underground structures are susceptible to be damage under cyclic loading.

In the past decades, many researchers have focused their research on the understanding of the dynamic tunnel response subjected to the seismic load. Hashash et al. [4] reported a summary of the seismic underground structures design, the current understanding on the seismic behaviour of underground structures and the demand for further research. This state-of-the-art review has been updated by Tsinidis et al. [5]. Seismic loading on tunnels can lead to two major safety concerns, namely the soil-structure-interaction (SSI) effects such as tunnel lining structural damages due to the seismic inertial forces; and in loose, saturated soils, the floatation of buried structure due to the generated excess pore pressures within the soil. Seismic tunnel response has been investigated using both physical modelling and numerical analyses. Cilingir and Madabhushi [6] studied square tunnel lining response and earth pressures with different tunnel lining flexibility in dry, loose sand. The circular tunnel response is also studied by Cilingir and Madabhushi [7,8]. However, it should be noted that most of the underground structures are not constructed in free field condition but located in congested urban areas in the proximity of other surface structures. It is necessary to consider a variety of surcharge load distribution at the surface, such as different types of the building foundation, and the road pavement to simulate a more realistic scenario. Earthquake-induced building settlements have been widely investigated by Dashti et al. [9,10]. This work built the basis of understanding the dynamic building behaviour without any underground structures. Dashti et al. [11] and Hashash et al. [12] investigated the influence of both midrise and high-rise structures on the adjacent underground braced excavations during the earthquake through a series of centrifuge tests and 3D numerical modelling. This research is quite important during the construction phase of a project where the braced excavations are

* Corresponding author.
E-mail address: za301@cam.ac.uk (Z. He).

https://doi.org/10.1016/j.soildyn.2024.108693
Received 9 November 2023; Received in revised form 31 March 2024; Accepted 30 April 2024
Available online 14 May 2024

vulnerable. Results presented the criticality of the building induced lateral load to the underground structures seismic response and the non-linearity of the loading distribution. Bilotta et al. [13] studied the dynamic behaviour of the shallow tunnel structures adjacent to existing surface buildings as part of the SERA project, and this work has been extended by Miranda et al. [14] with a series of the dynamic centrifuge testing.

Tunnels are also vulnerable when located in loose, saturated soils due to the occurrence of soil liquefaction. Tunnel floatation due to horizontal cyclic loads in saturated soil has been widely observed from the dynamic centrifuge testing by Chian and Madabhushi [15]; the 1-g shaking table testing by Watanabe et al. [16] and Taylor and Madabhushi [17]; and the 2D finite element analysis for rectangular tunnels by Madabhushi and Madabhushi [18]; and for circular tunnels by Chian et al. [19]. Chou et al. [20–22] tested the uplift of a cut-and-cover tunnel in the BART Transbay Tube (TBT) project at California, using centrifuge testing and considered a geologically realistic soil profile. Due to the variety of the soil properties along the longitudinal tunnel profile, two centrifuge tests conducted in the BART projects have implemented two different free-field soil material and considered the differentiation of the refill soil property to simulate a more realistic construction sequence. Adalier [23] and Yang et al. [24] assess the seismic design of the George Massey Tunnel at Vancouver through a series of centrifuge tests and 2D numerical modelling. The model tunnel had a thin layer of asphalt above the crown but without any overburden soil to simplify the field conditions. The static factor of safety against floatation can be determined to be ~1.06 by considering the aluminium model self-weight, buoyancy force and the sidewall soil interface frictional resistance. Their test results establish the efficacy of ground densification and gravel drainage zones in mitigating the liquefaction induced uplift of this very buoyant tunnel. Pore pressures in the soil body are built up during the earthquake as expected, leading to full or partial liquefaction. The floatation is even more serious when the tunnels are buried at shallow depth due to the low vertical resistance against uplift.

This research aims to investigate the floatation mechanism of a shallow cut-and-cover rectangular tunnel, and the interaction between the tunnel, soil, and adjacent building foundation during the strong horizontal cyclic loading, through a series of the geotechnical dynamic centrifuge tests and 2D numerical modelling. One of the novelties of this research is the use of high-speed image and PIV analysis to observe soil deformation around the tunnel and under the foundation during seismic loading. In this research, the tunnel is buried with an overburden soil layer present above the crown, as would be the case in many practical applications.

2. Centrifuge modelling

Geotechnical centrifuge modelling is a well-established tool to investigate underground structures in many previous research projects. It can simulate similar prototype soil non-linear stress and strain conditions in a 1: N scaled down model by centrifugal accelerating the model in N g-level, following the scaling laws shown in Table 1. Schofield [25]. proven the model soil stress error in the centrifuge is acceptable. Three dynamic centrifuge models are tested in the Turner beam centrifuge with a rotational radius of 4.125 m at the Schofield Centre, Cambridge University. Testing g-level was 60 g for all three tests. Further concepts of the Geotechnical centrifuge operation and details of the Turner beam centrifuge are described by Schofield [25] and Madabhushi [26]. It must be noted that other scaling relationships such as Iai et al. [27] are reported literature for 1-g shaking table tests. These are not applicable to dynamic centrifuge tests where gravity is scaled by factor of N to obtain prototype stress and strain. Iai et al. [27] do not scale gravity but instead scale stress and strain differently.

Table 1
Scaling laws for centrifuge tests, Schofield [25].

Parameters	Model/Prototype	Dimensions
Length	1/N	L
Mass	$1/N^3$	M
Stress	1	$ML^{-1}T^{-2}$
Strain	1	1
Force	$1/N^2$	MLT^{-2}
Seepage velocity	N	LT^{-1}
Time (seepage)	$1/N^2$	T
Frequency	N	LT^{-1}
Acceleration	N	LT^{-2}
Velocity	1	LT^{-1}

Note: N, scaling factor.

2.1. Structural design

This research aims to study the dynamic response of a shallow rectangular cut-and-cover tunnel adjacent to the building structures subjected to earthquake loading. The model tunnel is designed to simulate a two-lane twin rectangular cut-and-cover tunnel with single square section of 6 m × 6 m at the prototype scale. This dimension is commonly seen in the design of one-lane passage motorway tunnel. The tunnel structure is manufactured by gluing two 100 mm × 100 mm aluminium square hollow sections with 2 mm thickness. Tunnel lining is modelled as 120 mm thick aluminium plates at the prototype scale, which is equivalent to 300 mm thick concrete sections with equivalent bending stiffness. The flexural stiffness (EI) and axial stiffness (EA) of the tunnel section at the prototype scale are 2.568×10^6 MN m^2/m and 4.113×10^5 MN/m, assuming the concrete stiffness as 25 GPa and the aluminium stiffness as 70 GPa. The cross-sectional views of the tunnel at the prototype and model scales are manifested in Fig. 1. Both edges of the tunnel are sealed and inserted into the polytetrafluoroethylene (PTFE) plates to reduce the transverse friction between the tunnel model and the container. The PTFE inserts at the ends do not contribute to the structural stiffness of the model tunnel due to the flexible, silicone sealant used. The surface building structure has been simplified as a rigid raft foundation aluminium block with 100 mm span and 30 mm high. The block contact face has also attached with a 2 mm PTFE plate for the same purpose to reduce the transverse sectional friction. This block is equivalent to approximately 50 kPa surface surcharge to the beneath soil under 60 g. This contact pressure simulates the structural weight of a two-story residential building with raft foundation thickness of 0.5 m, width of 6 m and height of 7 m (3.5 m per story). No live load and designed loading combination are considered. A reference marker matrix is attached to both building and tunnel model to trace the structural and soil movements by adopting Particle Image Velocimetry (PIV) method. Fig. 2 presents the location of the tunnel and building model in test ZA03.

2.2. Test preparation

In this research, all three centrifuge tests are prepared with loose Hostun HN31 sand [28,29] by adopting an automatic sand pouring machine described by Madabhushi et al. [30]. The details of the sand property are shown in Table 2. Tests are placed in the window testing container that is manufactured by aluminium with a rigid Perspex observing window panel in the front face. Many previous researchers [15,19,6–8] have utilized this type of testing container to capture the buried structures behaviour through the Perspex with a high-speed camera. A servo-hydraulic shaker described by Madabhushi et al. [31] was used to apply the earthquake input motion to the centrifuge model. In order to minimize the wave reflection during the cyclic loading from the rigid container boundary, 30 mm thick deformable Duxseal are placed on both edges of the container that can approximately reduce at least 65 % of the boundary wave reflection [32]. A summary of the test configurations is shown in Table 3. A sinusoidal input motion with 10 cycles of shaking and peak ground acceleration (PGA) at the bedrock

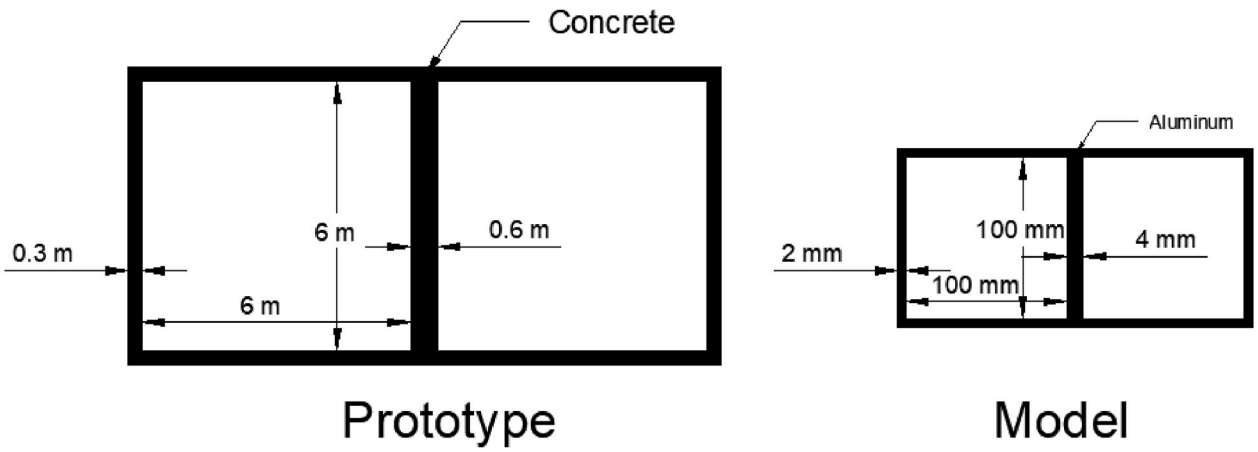

Fig. 1. Cross-sectional views of the prototype and model tunnels.

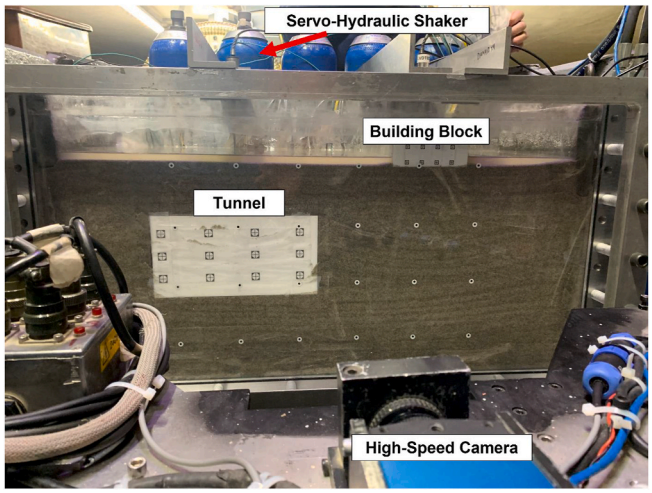

Fig. 2. Completed model of test ZA03 before spinning.

Table 2
Hostun sand material properties

Parameters	Value
φ_{crit} (degrees)	33[a]
D_{10} (mm)	0.209
D_{50} (mm)	0.335
e_{min}	0.555[a]
e_{max}	1.01[a]
G_s	2.65[a]
K (m/s)	1×10^{-3}[b]

[a] Data from Mitrani [29].
[b] Data from [28].

level of around 0.2 g is selected from the testing sequence to analyse the dynamic soil and structural behaviour. This input motion generates sufficient cyclic shear strain amplitude in the saturated soil to generate significant excess pore pressures, and the structures suffer floatation in the case of the model tunnel and settlement in the case of the raft foundation respectively. In Fig. 4, the input motions generated in each of the centrifuge tests are shown. The same input motions were used in the corresponding dynamic finite element analyses. The input motions were applied to the numerical model at the base nodes as an acceleration-time history to ensure direct comparison of the numerical results with the centrifuge test data.

For two saturated tests ZA02 and ZA03, the sand is saturated with high viscous methyl cellulose fluid that are prepared at the designed viscosity (N = 60) for satisfying the model scaling law so that the rate of excess pore pressure generation and rate of pore pressure dissipation post-earthquake are matched [26]. Tunnel static factor of safety (FoS) against floatation are determined as 1.46 for ZA02 and 1.17 or ZA03 by adopting a simplified vertical FoS equation shown in eq [1], where F_B is the tunnel buoyant force, F_T is the tunnel structural self-weight, F_{Soil} is the soil effective overburden stress. This is a preliminary determination to ensure the designed tunnel buried depth is reasonable, that the tunnel should not float under static conditions.

$$FoS = \frac{F_{Soil} + F_T}{F_B} > 1 \quad [1]$$

The soil shear contribution of a monotonic pipe has been investigated by assuming two vertical slip surfaces on the pipe edge [33,34], and been improved by including the soil dilation effect [35]. However, the slip surface for the rectangular shape tunnel is still under investigation. The preliminary FoS calculation in this series of centrifuge tests did not consider the slip surface frictional resistances by assuming the tunnel aluminium sidewall friction is neglectable, therefore the static FoS is underestimated.

Four types of instruments are installed in the tests, as shown in Fig. 3. Piezo accelerometers are buried in the free field (under the building block for ZA03), and adjacent to the tunnel lining to obtain the dynamic soil shear wave propagation during the earthquake. The

Table 3
Centrifuge tests configurations

Earthquake ID	Earthquake				Building Block		Tunnel Buried Depth	Soil	
	Type	Frequency (Hz)	Duration (s)	Peak acc. (g)	Installation	Distance to Tunnel		Saturation	RD (%)
ZA01_EQ4	Sinusoidal	1	~10	0.24	No	–	0.75D	Dry	49 %
ZA02_EQ3	Sinusoidal	1	~10	0.21	No	–	0.75D	Saturated	41 %
ZA03_EQ2	Sinusoidal	1	~10	0.21	Yes	1D	0.5D	Saturated	43 %

Note: D = 100 mm.

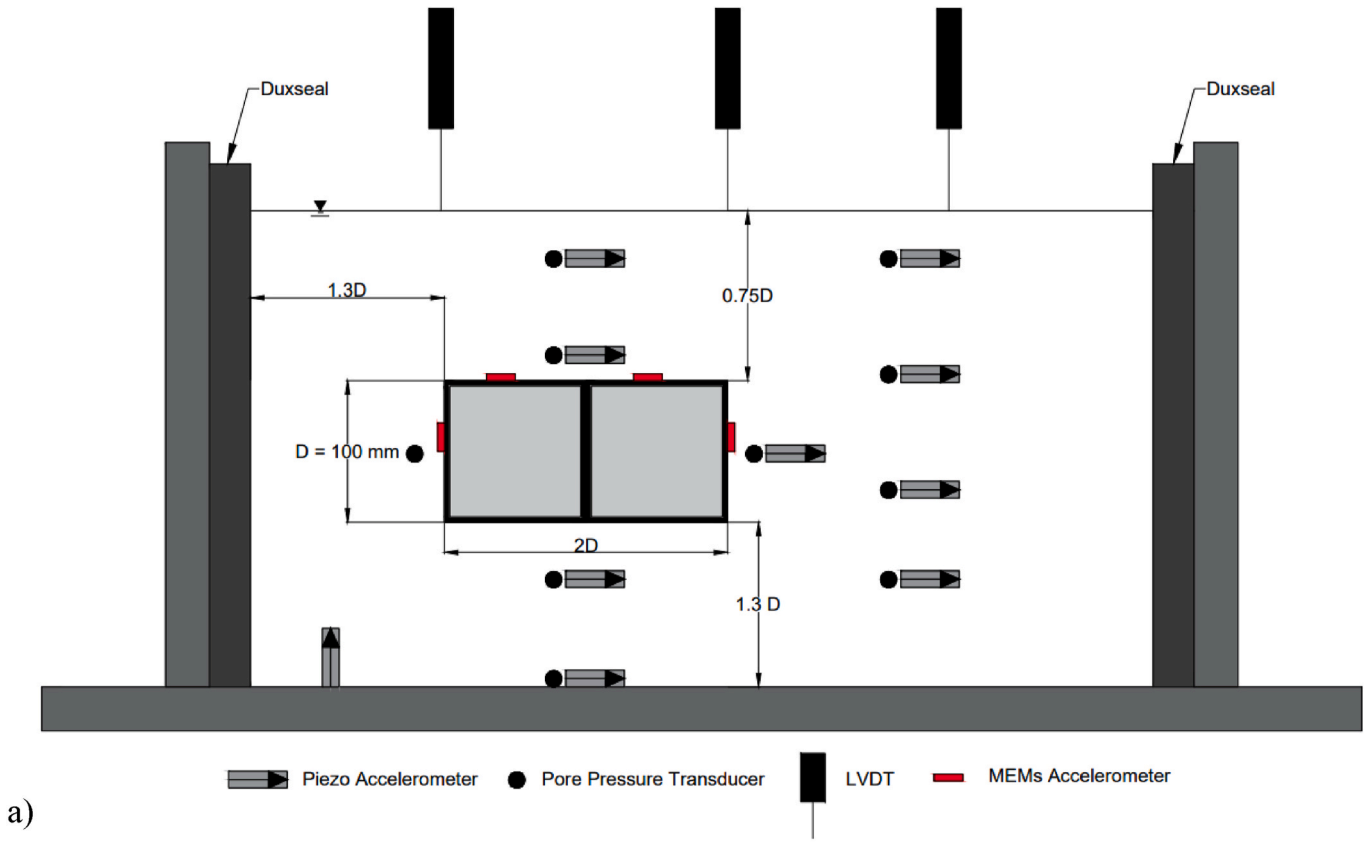

a)

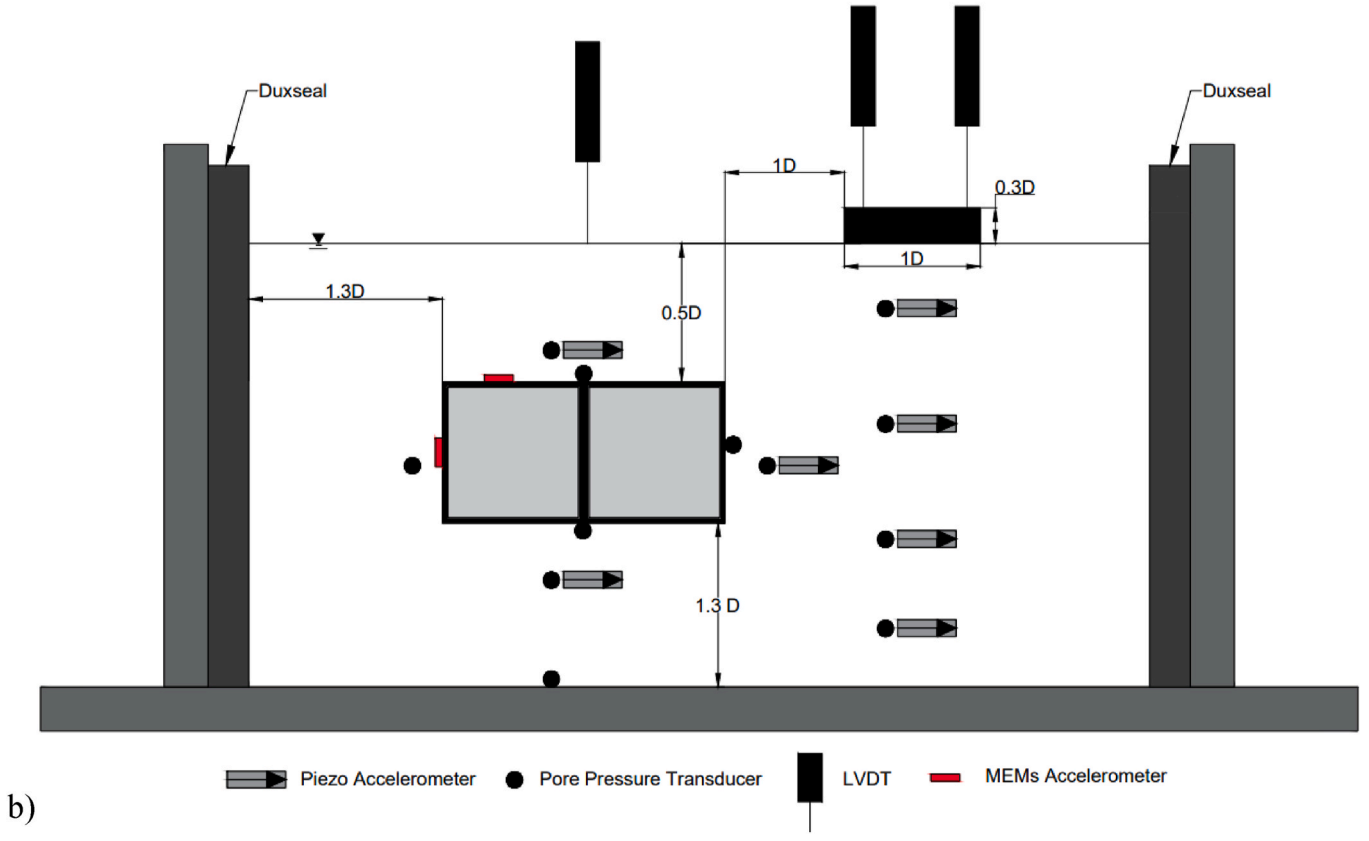

b)

Fig. 3. Typical centrifuge model layouts: a) without building block for ZA01 and ZA02; b) with building for ZA03.

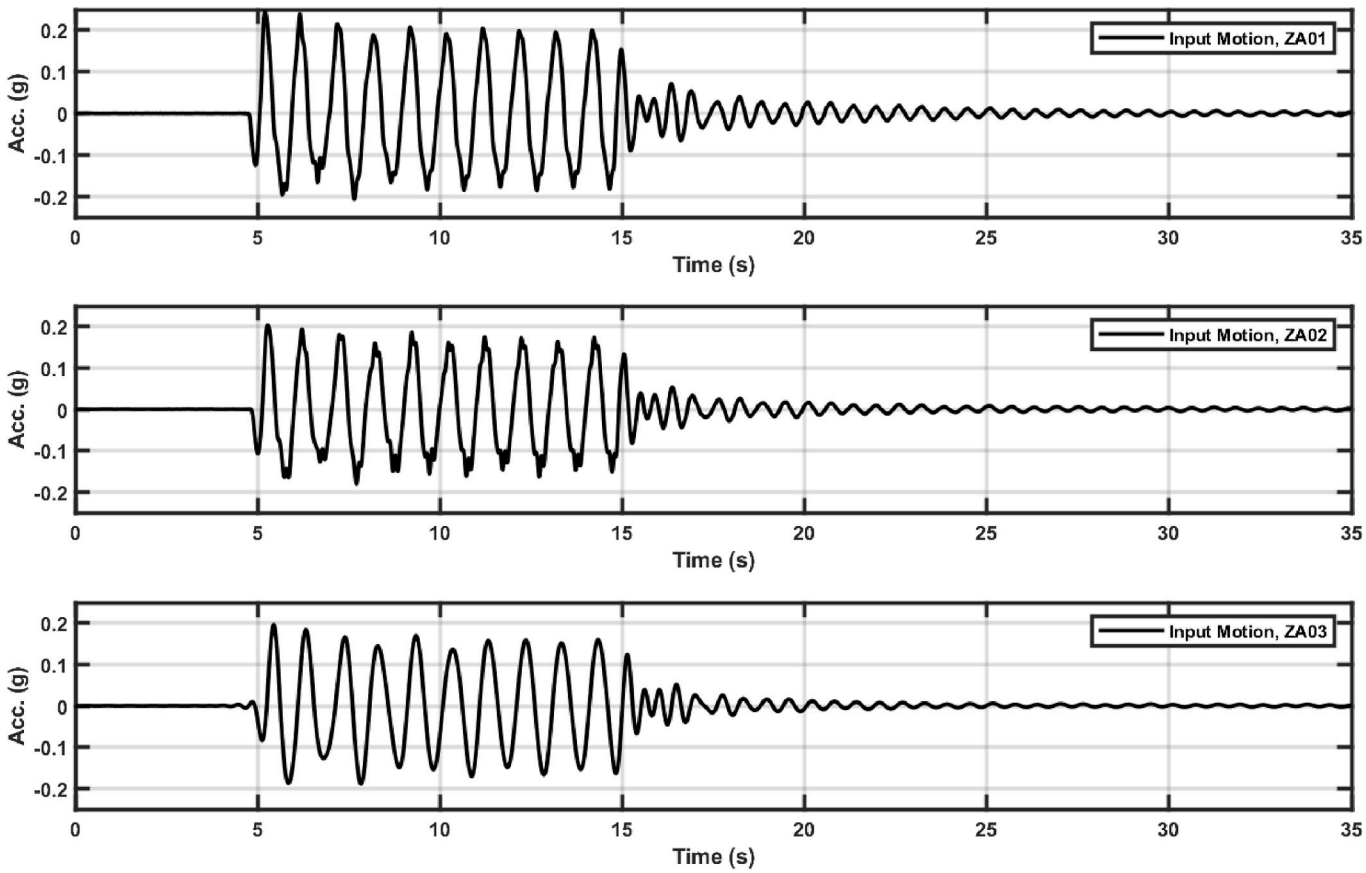

Fig. 4. Sinusoidal input motions applied to the centrifuge tests ZA01, ZA02 and ZA03.

micromechanical system accelerometers (MEMs) are attached on the tunnel crown and sidewall to capture the tunnel structural acceleration and the rotation. The linear variable differential transformers (LVDT) are placed on the ground surface and top of the building block (for ZA03) to obtain the surface ground movement and the building settlement. The pore pressure transducers (PPT) are buried (for ZA02 and ZA03) adjacent to piezo accelerometers and attached along the tunnel lining to capture the excess pore pressure in the sand. In addition, the Particle Image Velocimetry (PIV) technique is implemented to trace the soil, tunnel and building movements. This involves a high-speed camera fixed in front of the Perspex, and an image-based MATLAB script GeoPIV_RG [36].

3. Numerical modelling

Numerical modelling based on finite element analyses in time domain has been proven as an effective tool to undertake complex geotechnical and SSI problems. The current study presents the numerical analyses carried out using a 2D generalized plasticity based finite element code SWANDYNE under plane strain assumption, developed by Chan [37]. This formulation is based on the unconditionally stable generalized Newmark method that solves the fully coupled Biot's equations. Details of the functionality of the SWANDYNE code are comprehensively described by Madabhushi and Zeng [38], Madabhushi and Madabhushi [18].

The finite element discretization is conducted in four distinct zones,

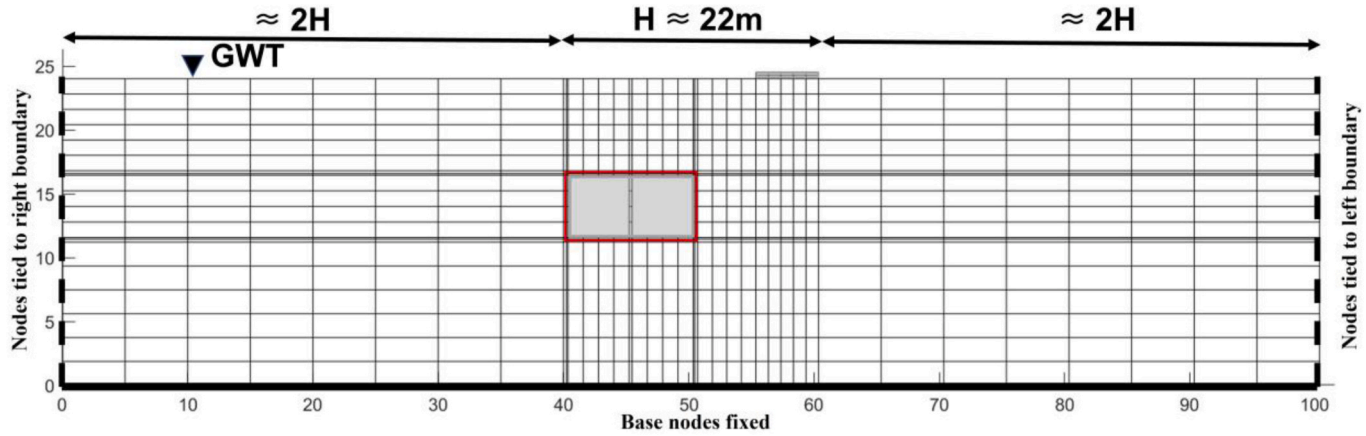

Fig. 5. Typical FE mesh discretization with applied boundary conditions.

namely the loose sandy soil stratum, the soil-tunnel interface elements, the rectangular tunnel transverse section, and the building block as shown in Fig. 5. All elements are quadrilateral with 8 solid nodes with 9 Gauss points each, for capturing the displacements and accelerations at solid nodes and in-situ stresses and strains at the gauss points. A reasonable dense gridding partition is considered close to the tunnel and the surrounding foundation soil to minimize numerical integration errors. The free field extends more than twice the width of the tunnel-building system to avoid any boundary effects due to wave reflections. However, in the free field the mesh density is reduced to have optimal computational efficiency. Slip elements were used at the tunnel-soil interface. For saturated analyses, each soil element has 4 additional fluid nodes overlain on corner solid nodes to create a fluid mesh to determine the pore pressures. Solid nodes along the bottom of the model are fully fixed in both horizontal and vertical directions. This enables the input motion to generate vertically propagated shear wave from the base of the model. The model side boundaries with the same y-coordinates are "tied" together, which means they experience the same displacement and acceleration.

Haigh et al. [39] investigated the effect of different time steps in capturing the non-linear dynamic saturated soil behaviour and recommended that the error will be reduced to less than 5 % if there are more than 10-time steps are used for the shear wave to traverse the smallest discretized element. The time step adopted in this study is 0.1 ms by assuming an average soil shear velocity of 150 m/s, which takes approximately 10 times more travel time to propagate shear wave through the smallest finite element.

3.1. Constitutive models

It is important to capture the key features of the cyclic behaviour, such as the excess pore pressure generation, liquefaction, and permanent deformation. A generalized plasticity bounding surface model P-Z Mark III model (defined as DEP08F model in SWANDYNE [37], developed by Paston et al. [40]; is implemented in the dynamic time step analysis. This model has been widely used by previous researchers [37,39,38] in studying the dynamic saturated soil response. The P-Z Mark III model defines the plastic potential in eq [2], where the p' is the mean effective stress; q is the deviatoric stress; M_g is the slope of the critical state line (CSL), which is regarding the soil friction angle and Lode's angle; $\propto_g$ and p_g are constant.

$$G\left(p',q,p_g\right)=\left\{q-M_g p'\left(1+\frac{1}{\propto_g}\right)\left[1-\left(\frac{p'}{p_g}\right)^{\propto_g}\right]\right\} \quad [2]$$

The model yield surface is assumed to have the same shape as the plastic potential surface and therefore is defined similar to eq [2] but with another group of parameters, - namely M_f, $\propto_f$ and p_f. Parameters β_0 and β_1 are adopted to calculate the plastic modulus during the loading period, and the parameter γ_{Hu} is adopted to calculate the plastic modulus during the unloading period. Details of model parameters is shown in Table 4 and have been fully explained by Zienkiewicz et al. [41]. The values adopted for the current analyses were based on previous work on shallow tunnel floatation by Madabhushi and Madabhushi [18]. Rayleigh damping is considered in this numerical analysis with mass and stiffness matrix coefficients as supplemented in Table 4. Same Rayleigh damping coefficients were used in the LEAP-GWU projects that can give about 20 % of damping ratio for the driving frequency of 1 Hz [42]. Other recently developed constitutive models for the geotechnical earthquake engineering, such as the SANISAND model developed by Dafalias and Manzari [43]; and the PM4SAND model developed by Boulanger and Ziotopoulou [44] are recommended for the further development and comparison.

Table 4
Parameters adopted in the P-Z Mark III model

Parameters	Symbol	Value
Slope of the CSL for plastic potential	M_g	1.15
Slope of the CSL for yield surface	M_f	0.85
Dilatancy parameter for plastic potential	$\propto_g$	0.45
Dilatancy parameter for yield surface	$\propto_f$	0.45
Plastic modulus on loading (Pa)	$H_{loading}$	600
Plastic modulus on unloading (Pa)	$H_{unloading}$	4×10^6
Permanent deformation parameter during unloading	γ_{Hu}	2
Permanent deformation parameter during reloading	γ_{DM}	0
Shear hardening parameter 1	β_0	4.2
Shear hardening parameter 2	β_1	0.2
Size parameter 1	p_f	0.5
Size parameter 2	p_g	0.5
Rayleigh damping coefficient	α	3
Rayleigh damping coefficient	β	0.05

4. Dynamic soil response

4.1. Soil acceleration time history

The measured free-field soil accelerations time history with corresponding Fast Fourier Transforms (FFTs) at different depth for test ZA01 and ZA02 are shown in Fig. 6. In this figure, the frequency content of the input motion remains unaltered at different depths in both dry and saturated sand. In the saturated test, the soil response at shallow depth has reduced significantly after the first 2 cycles of shaking. This is an evidence that the soil is liquefied and therefore it is harder to transfer any shear waves once liquefaction has occurred. In the dry test, as the horizontally polarized shear (S_h) waves propagate upwards towards the soil surface, they amplify with an amplification factor of around 1.3 between the bedrock and the soil surface. This can be seen as a higher peak response at frequency of 1Hz shown in the FFT plots. Comparing soil response in test ZA01 and ZA02, it can be seen that the accumulation of excess pore pressures in the soil medium plays a significant role in effecting the propagating shear waves, as expected.

The comparison between the numerical simulated soil horizontal acceleration time history and the centrifuge test output are discussed for test ZA03 and presented in Fig. 7. The acceleration time history recorded at the base of the centrifuge test container is adopted as the input motion of the numerical model. A good agreement is observed between the centrifuge test results and the numerical simulation outputs, both in term of the horizontal acceleration amplification and the frequency content. The reduction of the saturated soil wave propagation has been successfully captured in the numerical model, this proves the efficacy of the FE code with the corresponding constitutive model in simulating the realistic soil dynamic response.

The existence of the building foundation on the surface nearby causes a significant difference in the soil liquefaction ratio at the shallow depth. However, the additional constant overburden stress from the building block self-weight does not mitigate the reduction of the soil dynamic response. This is supported by Fig. 8, where the soil shear wave propagation and the excess pore pressure generation below the building location are compared. It can be observed that the soil is fully liquefied in test ZA02, as the excess pore pressure is approximately equal to the residual effective stress shown in the black dashed line. In contrast, the soil in test ZA03 does not generate sufficient excess pore pressure to reach the full liquefaction (red dashed line) due to the presence of the building. The soil horizontal wave propagations show good agreement in both test ZA02 and ZA03 without the two peak initial spikes prior to occurrence of liquefaction. It is interesting to see that while the excess pore pressure below the building foundation only reached about half of the initial effective stress value, the shear wave propagation is severely impeded as reflected by the attenuated accelerations reaching the building foundation.

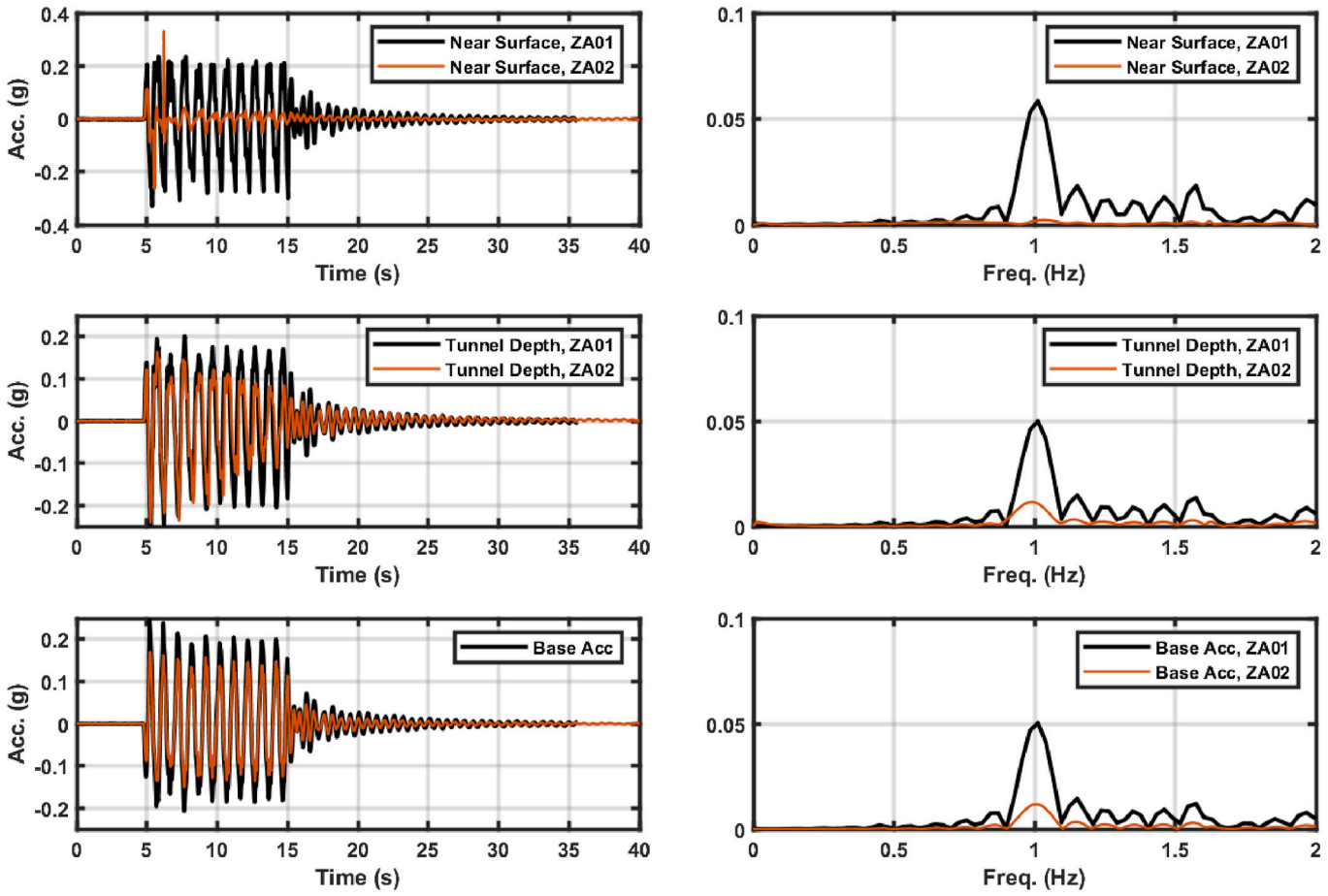

Fig. 6. Acceleration time history with corresponding FFT, test ZA01_EQ4 and ZA02_EQ3.

4.2. Excess pore pressure

Based on the classic soil effective stress principle by Terzaghi [45]; liquefaction can be defined as the reduction of the effective stress caused by the generation of excess pore pressures. These excess pore pressures are generated due to the tendency of soil to undergo volumetric contraction due to shear stresses under cyclic loading. A liquefaction ratio R_u introduced by Seed and Lee [46] is adopted to study the soil liquefaction at different depths. It is determined as the ratio between the soil excess pore pressure $u_{EX}(t)$ and the initial effective confining stress σ'_{v0} such that:

$$R_u(t) = \frac{u_{EX}(t)}{\sigma'_{v0}} \quad [3]$$

The liquefaction ratio beneath the building at the different depths for the test ZA02 and ZA03 are shown in Fig. 9. In this figure, it can be seen that the free-field soil near the surface and at the tunnel depth in test ZA02 is fully liquefied after the first 2 cycles of shaking, where the soil at the deeper depth with a higher confining pressure takes more cycles to accumulate sufficient excess pore pressure to be fully liquefy. In contrast, in test ZA03 the soil at the same locations but beneath the building are not fully liquefied due to the additional vertical loads from the building self-weight. This leads to the monotonic shearing movement of the soil as the building settles, inducing further dilatant behaviour from the soil. However, this phenomenon becomes less obvious at the deeper locations due to the reduction in the effect of surface surcharge with depth. This is indicated by the increase of the liquefaction ratio from around 0.55 near the surface to 0.71 at the model base. Fig. 10 presented the comparison of the shallow soil liquefaction ratio above the tunnel axis. The building-induced soil dilatant behaviour is also observed away from the building range due to the additional lateral earth pressure as the soil cannot reach fully liquefied with the presence of the adjacent nearby building.

The numerical simulation outputs are compared with the centrifuge data for the test ZA02 and ZA03, also shown in Fig. 9. The accumulation of excess pore pressures and the effect of the building vertical load are captured well in both tests. The soil liquefaction ratio shows good agreements with the centrifuge data. However, the rate of numerical excess pore pressure generation is slower than the centrifuge data. This aspect, while interesting, may not influence the final outcome substantially as the magnitude of excess pore pressures are captured well.

4.3. Soil deformations

Soil deformations and consequent tunnel movements are of primary concern for shallow tunnels in liquefiable soils. The soil deformations around structures are investigated by utilizing the Particle Image Velocimetry (PIV) technique. An image-based MATLAB script GeoPIV_RG designed by Stainer et al. [36] is adopted to analyse the model images obtained from a high-speed camera in front of the Perspex window (see Fig. 2). The cumulative soil deformation around the tunnel and the building (for ZA03) are presented in Fig. 11a and b. Based on these plots, it can be seen that the overburden soil above the tunnel crown has been pushed upward due to the tunnel floatation. For test ZA02 with a greater overburden depth and vertical floatation FoS, this soil uplift is accommodated in the soil above the tunnel, before reaching the soil surface. This is evidence that the saturated soil condition during the earthquake shaking is not fully undrained as there are plastic volumetric deformations occurring before the end of the earthquake. In test

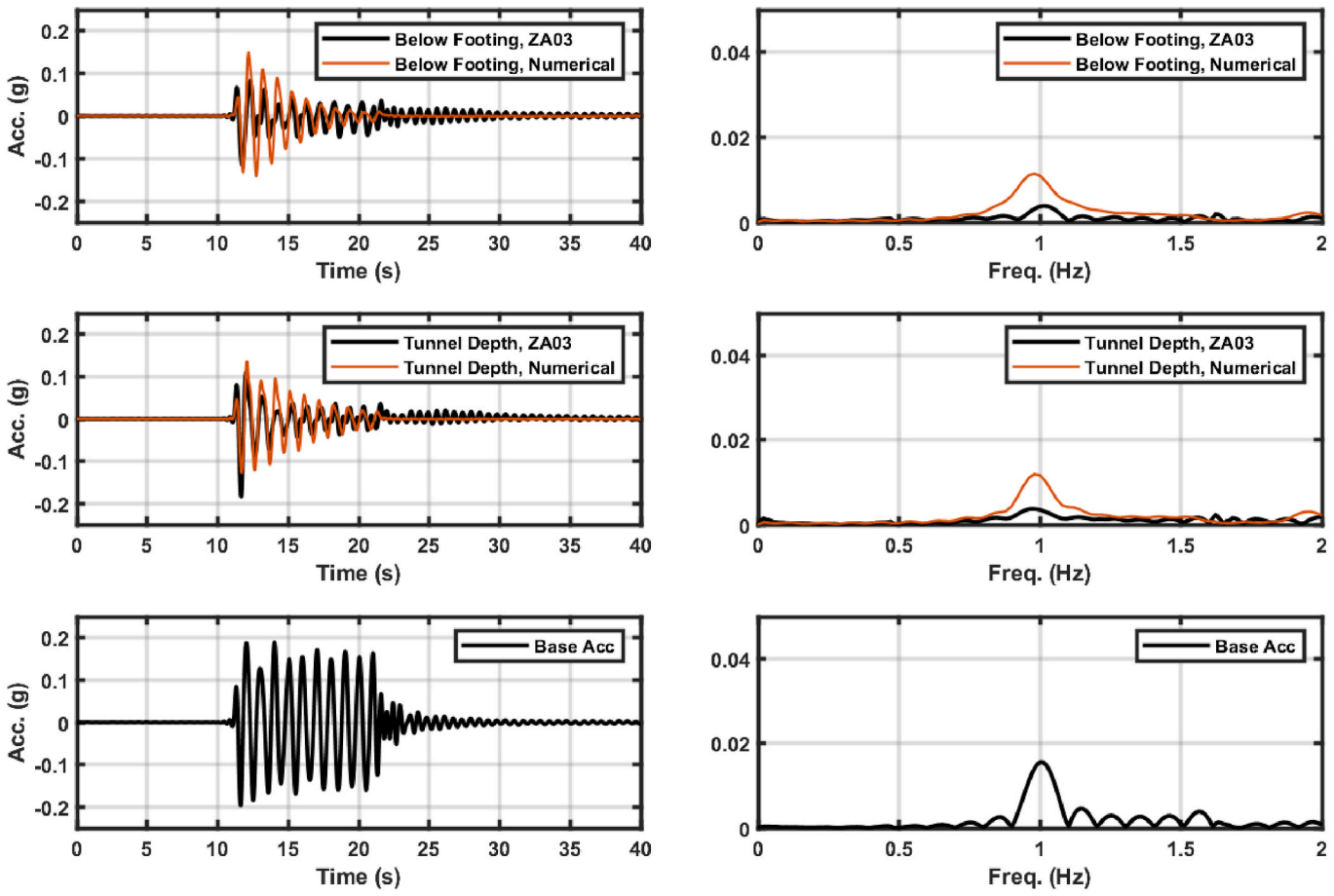

Fig. 7. Comparison of the acceleration time history with corresponding FFT for test ZA03_EQ2 and numerical model.

ZA03 with a lower floatation FoS and the smaller overburden depth, the soil above the tunnel moves upwards as seen in Fig. 11b. In addition, the soil at the bottom tends to fill the "gap" below the tunnel invert, which is presented by the circular loop on the right side of the tunnel. This leads to the soil dilation below the tunnel invert, and suction of the soil pore pressure.

The existence of the nearby building introduced significant soil settlement. An additional circular loop is formed around the top corner of the tunnel caused by the significant soil lateral movement, which can be observed in Fig. 11b. This can cause rotation of the building and the tunnel and will be discussed in the following sections. More lateral movements are observed along the tunnel right sidewall and indicated the tunnel has been pushed away from the building. This might lead to an increase of the soil lateral pressure, following an increase of the tunnel lining bending moments. Further PIV analyses also give the soil vertical deformation, which are presented in Fig. 12a and b. Soil densification has been encountered above the tunnel and below the building block. The presence of the tunnel has caused non-uniform building settlement and building rotation.

In addition, the soil shear strains are determined by discretizing the analysed image as a series of the triangular elements with a MATLAB script GEOSTRAIN_RG designed by Stainer et al. [36]. The soil linear cumulative shear strains after 4 cycles of shaking are presented in Fig. 13a and b. Note that the scales in these two figures are not the same. Significant soil shear strains are observed above the tunnel and along the tunnel sidewall for both tests.

Combining with the analyses of the soil deformations, it can be seen that the tunnel subjected to the earthquake loading can cause densification effect to the soil above the tunnel due to floatation and the soil along the tunnel sidewall due to the tunnel inertia force. The presence of the building significantly enhanced the soil shear movement along the tunnel sidewall. A shear band between the tunnel sidewall and the building is formed which indicates a change of the soil slip surface. Lateral soil movements are observed on the edge of the building, following the building rotation towards the tunnel axis. This failure mechanism is similar to the one proposed by Dashti and Bray [47] as the partial drainage during the earthquake affects the hydraulic gradients.

5. Dynamic structural response

5.1. Dynamic tunnel movement

Tunnel movements during the earthquake are investigated through the unique marker attached to the tunnel PTFE plate. Fig. 14 presents the trace of tunnel movement subjected to the sinusoidal input motion without and with the surface building. Amplifications of the tunnel movement through each cycle of shaking are successfully captured. Tunnel has cumulatively floated up to 0.11 m with the static vertical floatation FoS of 1.46 in test ZA02, and up to 0.24 m with the static vertical floatation FoS of 1.17 in test ZA03. This increase of the tunnel floatation with reduced cover depth is consistent with the observation from Chian and Madabhushi [15]. Tunnel has moved leftward by 0.05 m without building and around 0.11 m with building. This indicates that the tunnel has been 'pushed away' from the building, following an increase of the lateral earth pressure along the tunnel sidewall. Tunnel uplift time histories subject to the proposed sinusoidal input motions are shown in Fig. 15, and the numerical simulation outputs show in well match with the centrifuge observations.

In addition, the tunnel rotation time histories during the earthquake are investigated by determining the vertical movements of two attached

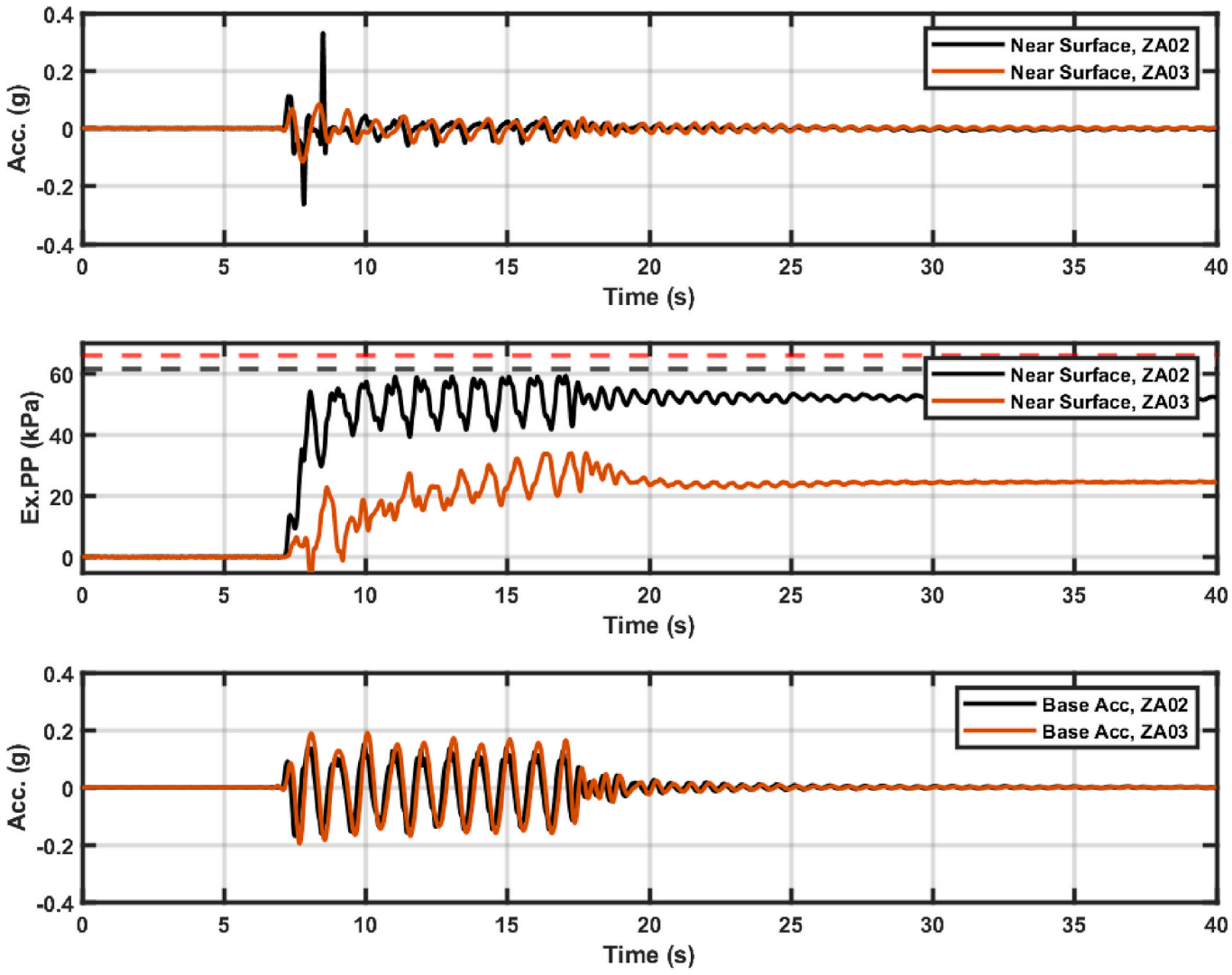

Fig. 8. Comparison of the soil horizontal acceleration, excess pore pressure time history beneath the building, test ZA02_EQ3 and ZA03_EQ2.

markers and presented in Fig. 16. During the earthquake, the tunnel rotates in the same direction in both tests (test ZA02 and ZA03). Maximum rotation has increased from 0.45° to 0.53° due to the presence of the building. This has also caused an increase of the residual rotation by a factor of 1.4. Such a difference proves the unbalanced surface surcharge exacerbates the tunnel rotation and lateral movement.

5.2. Tunnel floatation mechanism

It is necessary to investigate the force components acting on the tunnel during the earthquake in order to obtain a further understanding of the tunnel floatation. A simplified force mechanism acting on the buried rectangular tunnel is illustrated in Fig. 17. The tunnel buoyant force F_B is substantially greater than the tunnel structural self-weight F_T. This upward force is resisted by the soil effective overburden stress F_{Soil}, the soil shear contribution through the slip surface F_{SP}, and the tunnel sidewalls frictional contribution F_{SW}. This leads to the force equilibrium to ensure the tunnel is stable under static conditions, such that:

$$F_{Net} = F_{Soil} + 2F_{SP} + 2F_{SW} + F_T - F_B = Q_u > 0 \quad [4]$$

where Q_u is the soil bearing pressure beneath the tunnel invert. During a strong earthquake, the soil liquefaction-induced reduces the soil shear contribution F_{SP}. In addition, the excess pore pressure difference between the crown and the base can also contribute to the tunnel floatation. This is portrayed as an extra force component F_{EXPP} and can be determined as the difference between the excess pore pressure acting on the tunnel crown and invert, such that:

$$F_{Soil} + 2F_{SP} + 2F_{SW} + F_T < F_B + F_{EXPP} \quad [5]$$

$$F_{EXPP} = \int_{\frac{w}{2}}^{-\frac{w}{2}} f_{EXPP\_Invert} - \int_{\frac{w}{2}}^{-\frac{w}{2}} f_{EXPP\_crown} \quad [6]$$

where f_{EXPP} is the excess pore pressure distribution along the tunnel lining, w is the width of the tunnel. The vertical net force acting on the tunnel during the earthquake can then be determined as shown in Fig. 18. Tunnel vertical force equilibrium is discussed separately as three phases, namely:

i) static stage before applying the input motion.
ii) during the input motion
iii) post-earthquake residual stage

Excess pore pressures around the tunnel crown and invert are captured by two PPTs installed at these locations. Before the earthquake, the tunnel static net force is equal to the soil bearing pressure beneath the tunnel invert. This can be explained by the negative (downward) net force before the earthquake. During the earthquake, the soil bearing

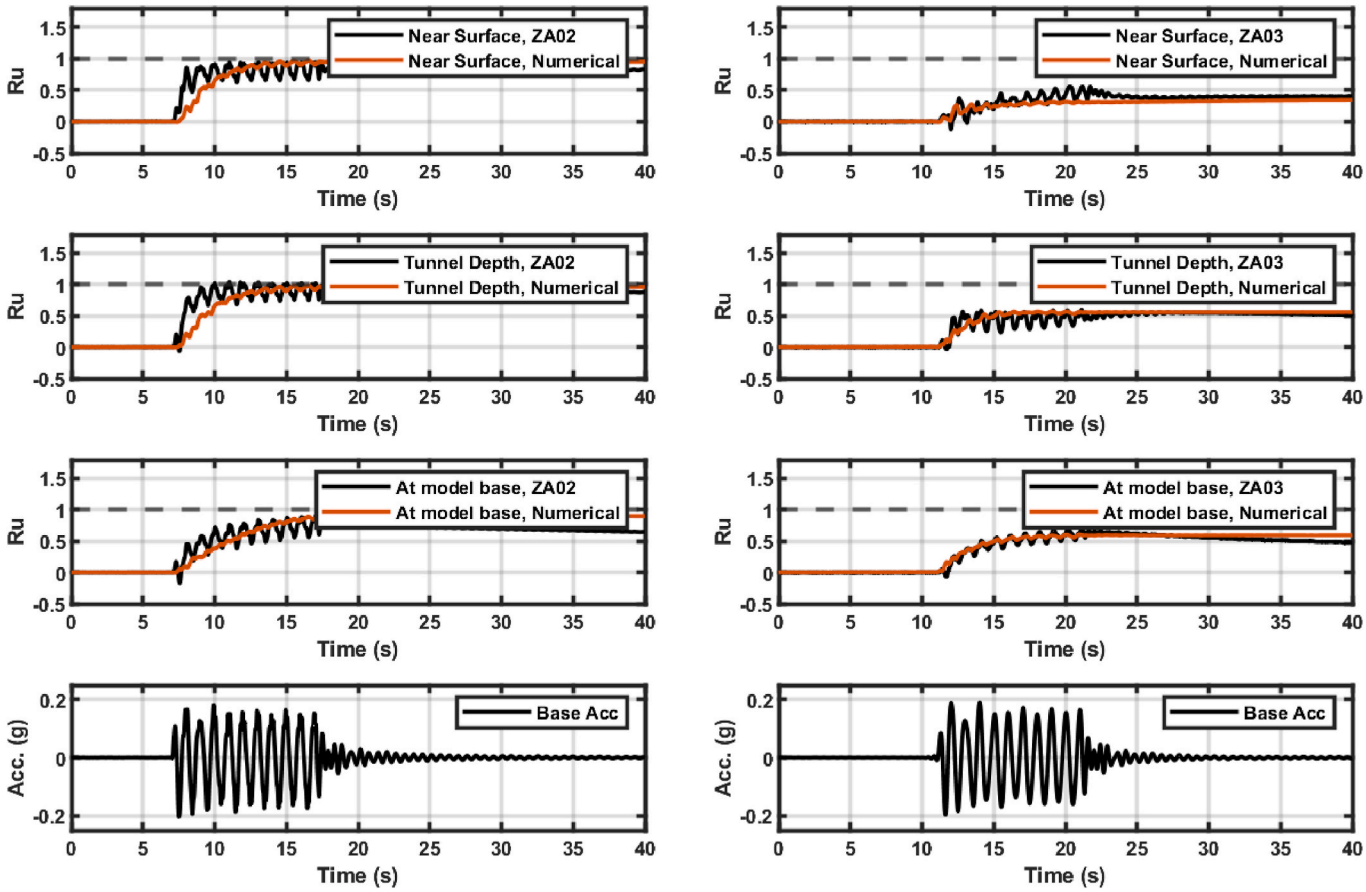

Fig. 9. Excess pore pressure time histories beneath the building for test ZA02 _EQ3 and ZA03_EQ2.

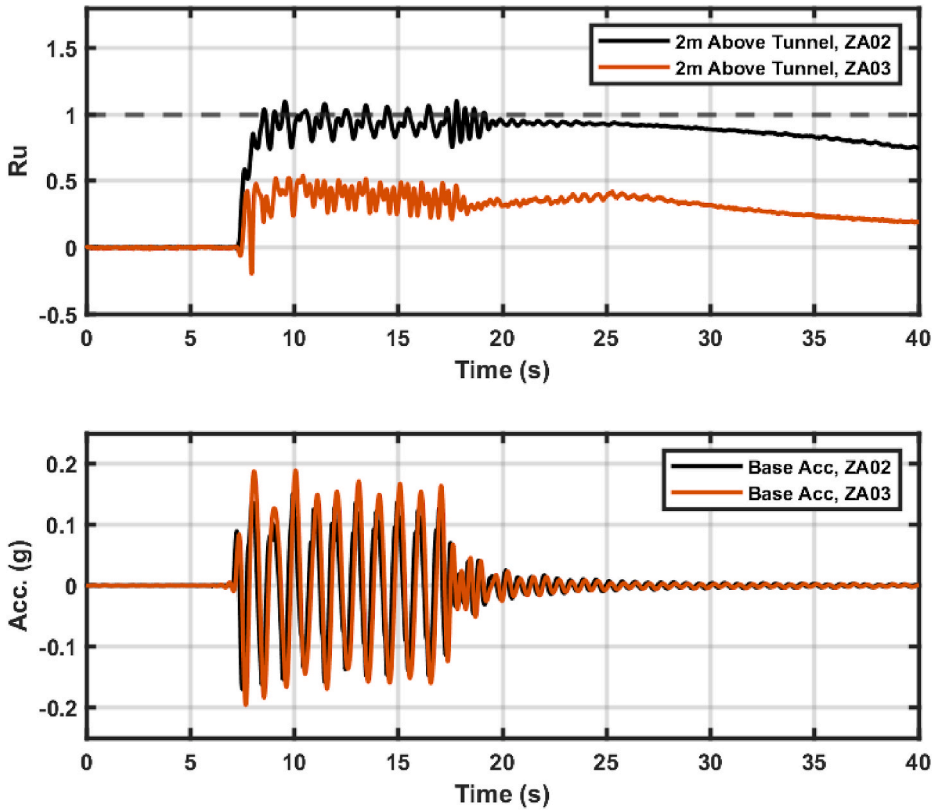

Fig. 10. Comparison of the soil liquefaction ratio above the tunnel for test ZA02 _EQ3 and ZA03_EQ2.

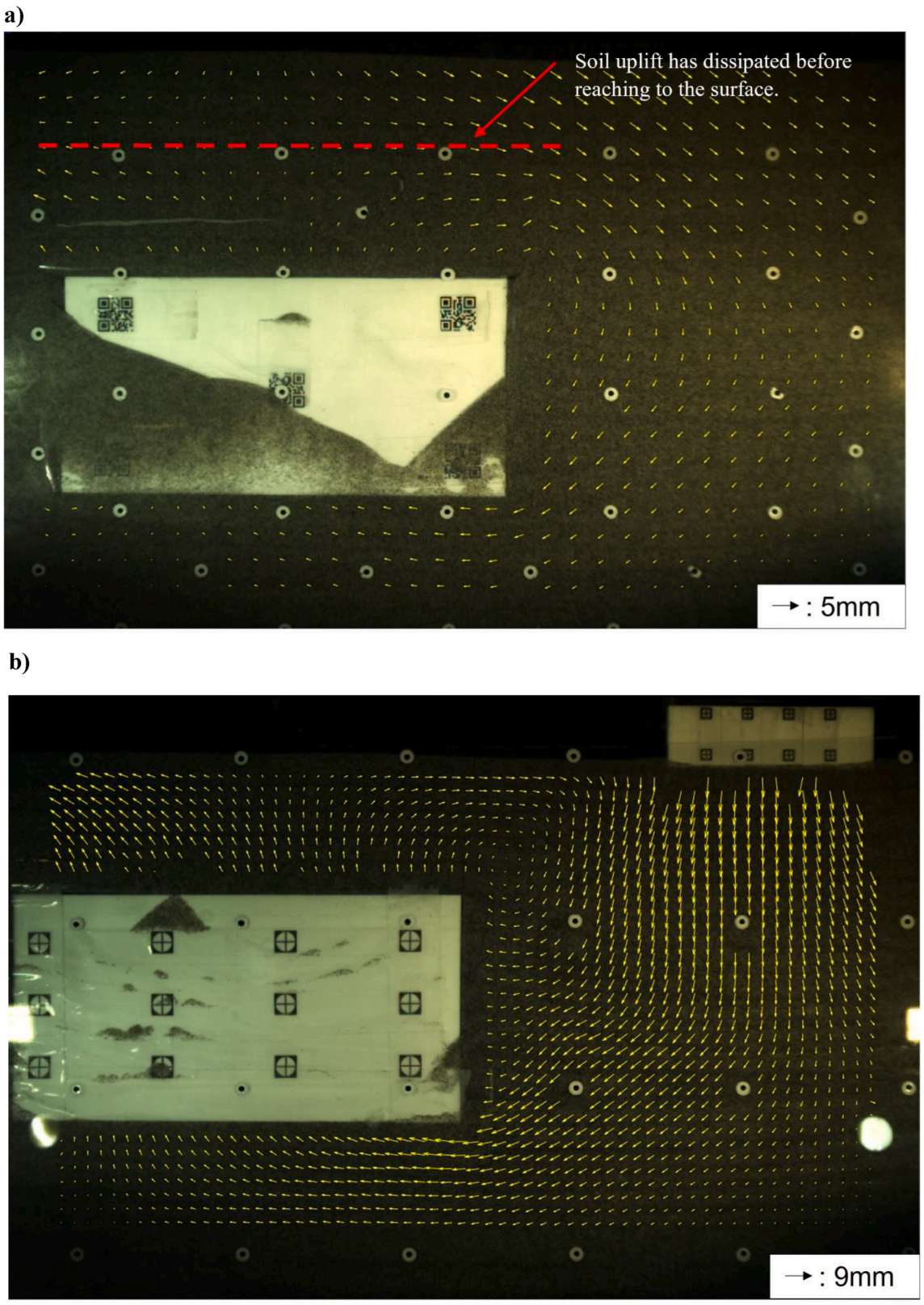

Fig. 11. Traces of soil displacements vector in the saturated soil (Model scale), a) without building (ZA02), b) with building (ZA03).

capacity is reduced to zero due to the tunnel floatation and the excess pore pressure generation. Significant excess pore pressure generation in the overburden soil layer occurs as seen in Fig. 9. It can be assumed that for test ZA02, the soil interparticle frictional structure is completely damaged due to the soil full liquefaction occurred during the earthquake, hence the frictional resistance along the slip surface F_{SP} is negligible during the earthquake. The net excess pore pressures vary, following the oscillation of the tunnel floatation. After the earthquake, the residual force component of the net excess pore pressure is less than the total vertical resistance since the tunnel self-weight and the soil

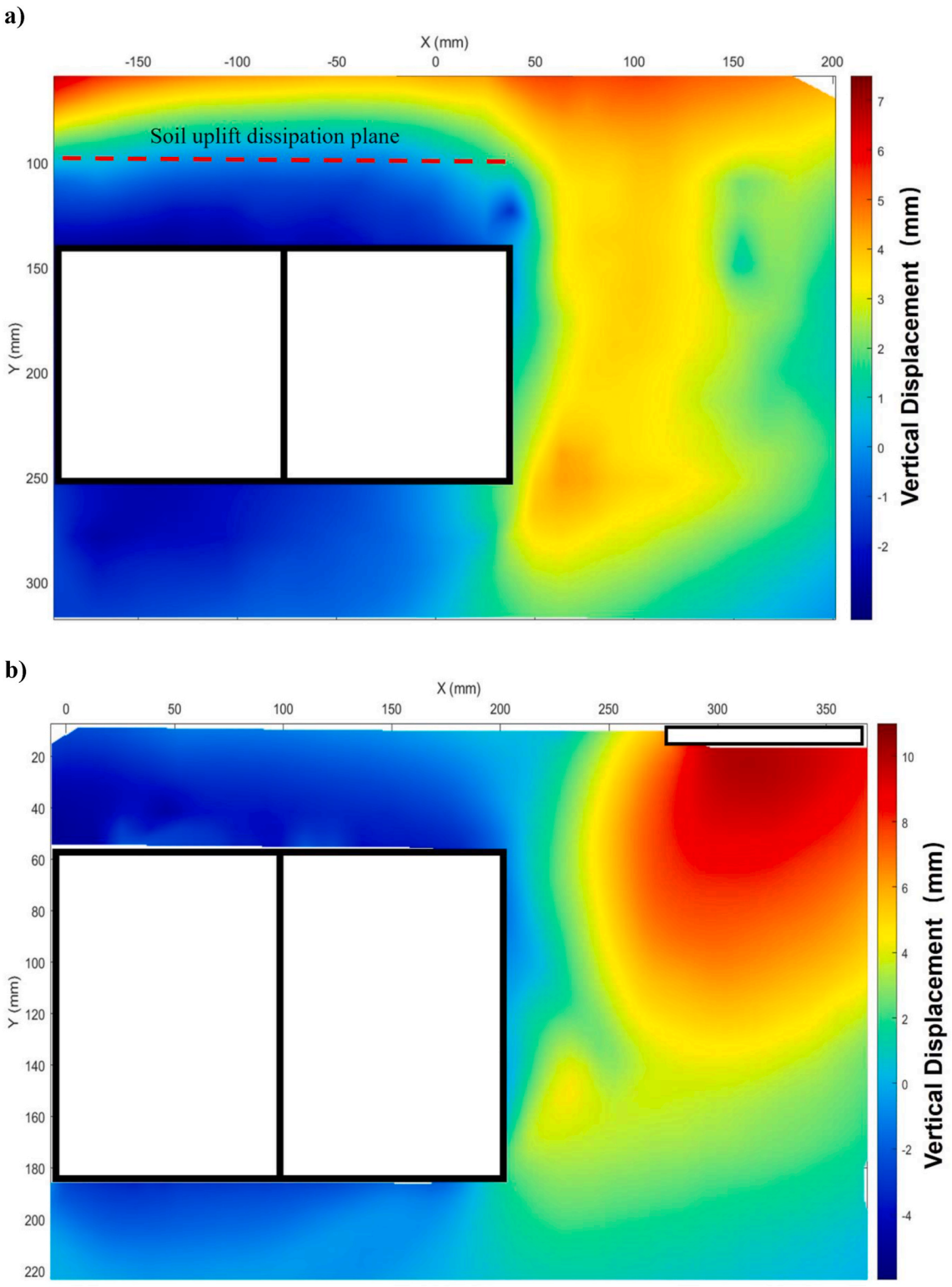

Fig. 12. Vertical displacement contour in the saturated soil (Model scale, positive as settlement), a) without building (ZA02), b) with building (ZA03).

overburden effective stress remain constant during the earthquake, which stops the tunnel uplift. It is expected that the slip surface frictional resistances and the soil bearing pressure will slowly recover with the drainage of the excess pore pressures.

5.3. *Dynamic building response*

Early research conducted by Dashti and Bray [47] show that the earthquake induced settlement of the building with the shallow foundation is primarily governed by the shear deformations from the structure-soil interaction and the partially bearing failure of the soil strength loss due to the soil liquefaction, as well as the partial drainage

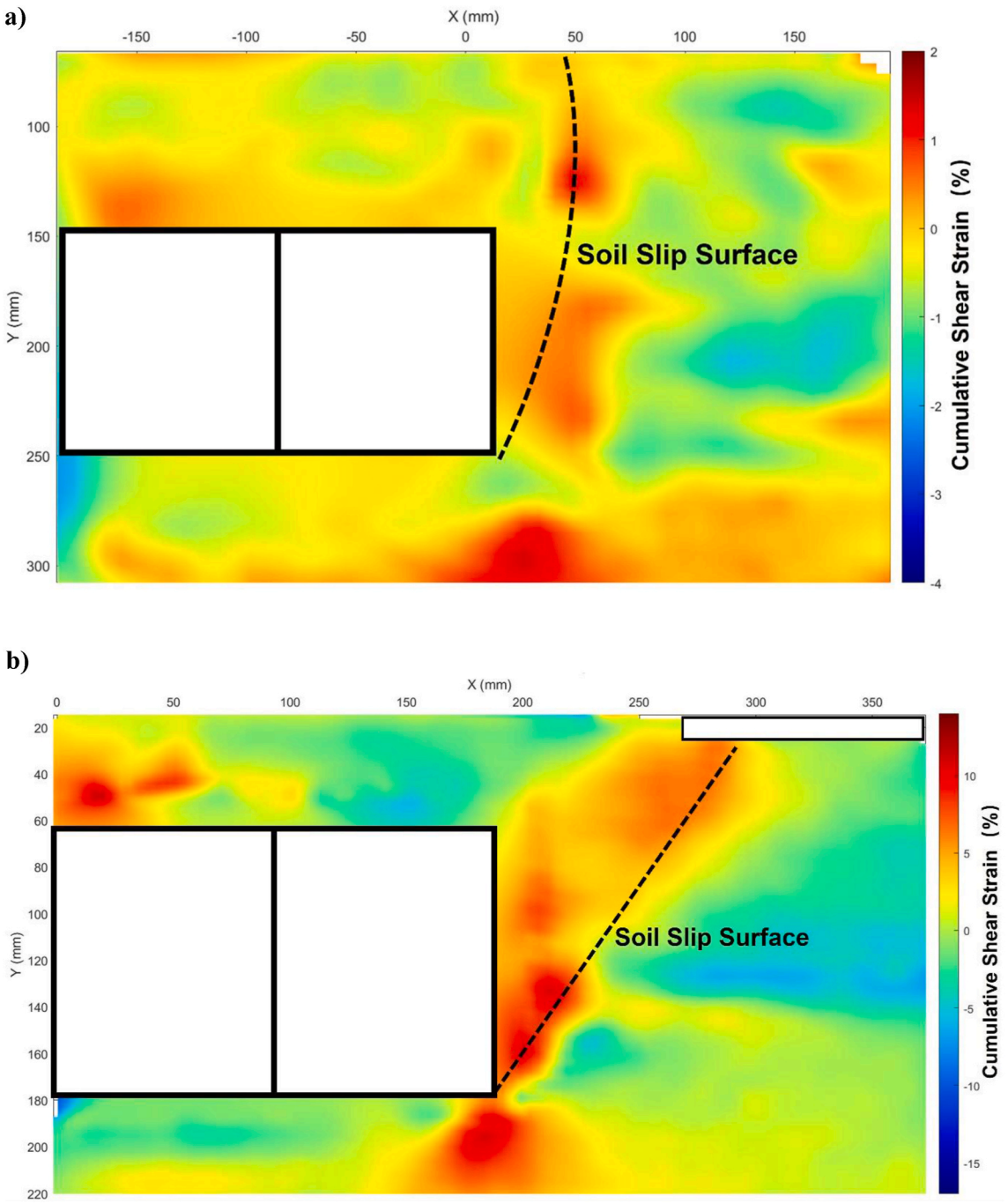

Fig. 13. Cumulative shear strain contour in the saturated soil after 4 cycles of shaking (positive as clockwise), a) without building (ZA02), b) with building (ZA03).

during the earthquake in effecting the hydraulic gradient. With the presence of the adjacent buried rectangular tunnel, dynamic building response also suffered by the building-tunnel interaction, as the tunnel floatation during the earthquake can significantly affect the soil deformation beneath the building.

Building settlement subjected to the earthquake loading are captured by the LVDT placed on the top of the building block and by analysing the attached marker on the PTFE with PIV technique. In summary, the building settlement and rotation time histories as well as the numerical simulated outputs are compared and manifested in Fig. 19. Building rotates towards the tunnel direction, and the numerical simulation shows good agreement with the centrifuge results. The maximum building settlement captured in the centrifuge test is around 0.62 m with a settlement difference of 0.12 m from the edge to edge of the building. Ishihara and Yoshimine [48] suggested that building settlement from 0.3 m to 0.7 m is categorized as extensive damage and can cause large cracks and spouting of sands. Furthermore, the building rotation due to the non-uniform distribution of the settlement will significantly exacerbate the structural damage and reduce the building safety factor.

The empirical graph suggested by Liu and Dobry [49] has been widely adopted in estimating the lower and upper limit of the surface structure settlements. Other methodologies developed for estimating the free-field settlement are also compared to the centrifuge results in Table 5. Adamidis and Madabhushi [50]. investigated the dynamic building response with different building width/liquefied soil depth ratio (B/D_L) and building-induced bearing pressures. The building implemented in this study has a B/D_L ratio of around 0.3 with bearing pressure of 50 kPa, which is similar with the centrifuge test OA04

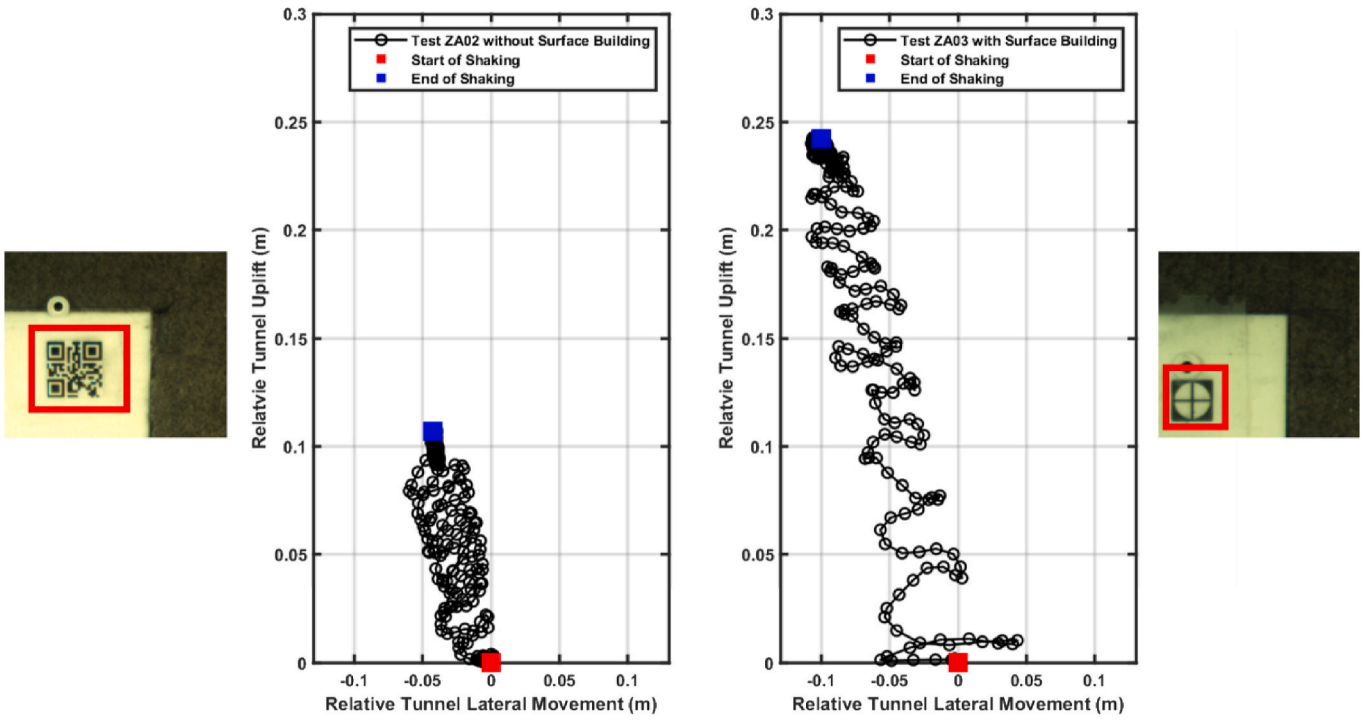

Fig. 14. Relative tunnel movement during the input motion (Prototype scale).

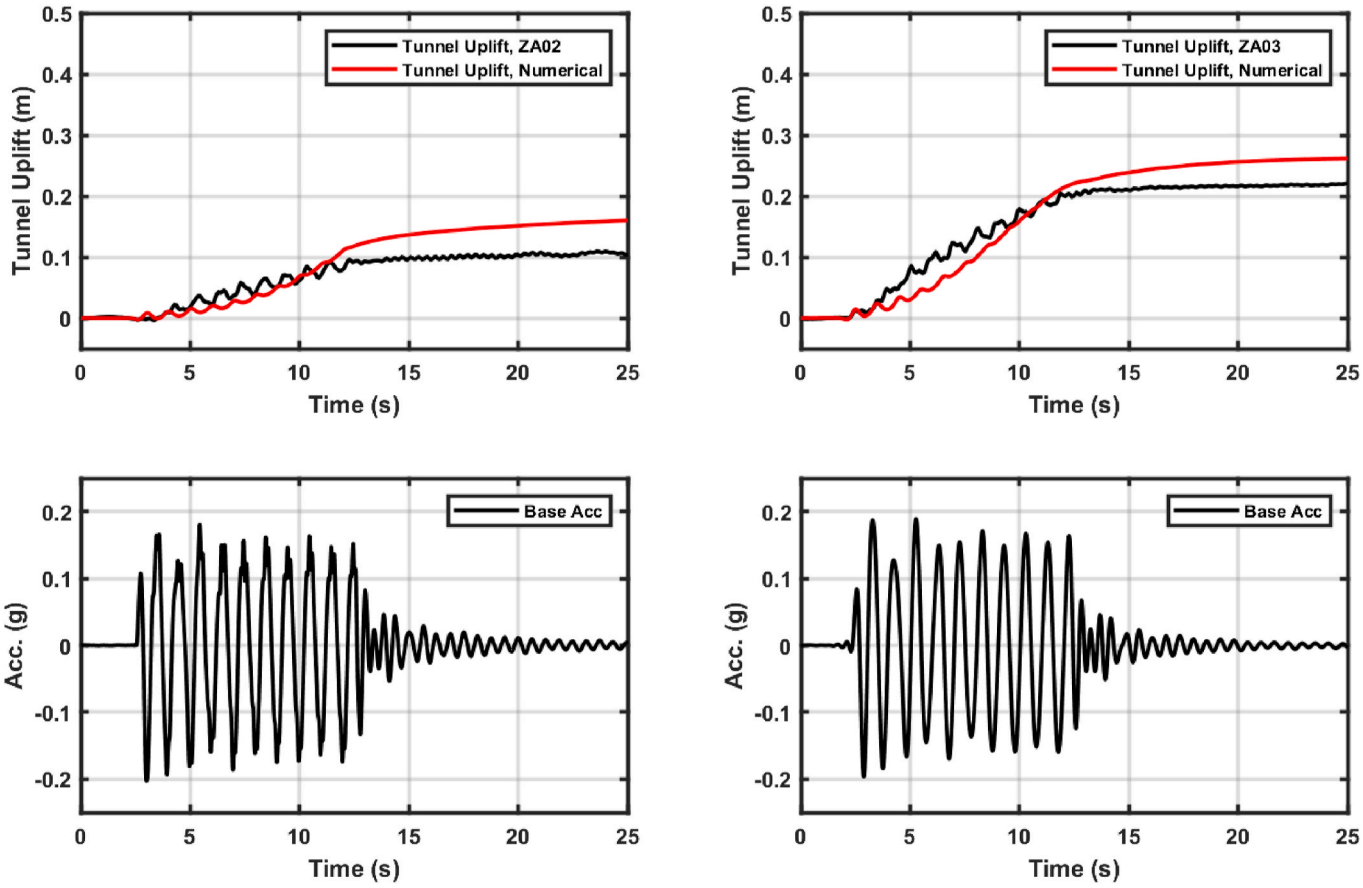

Fig. 15. Tunnel uplifts, test ZA02_EQ3 and ZA03_EQ2 (Prototype scale).

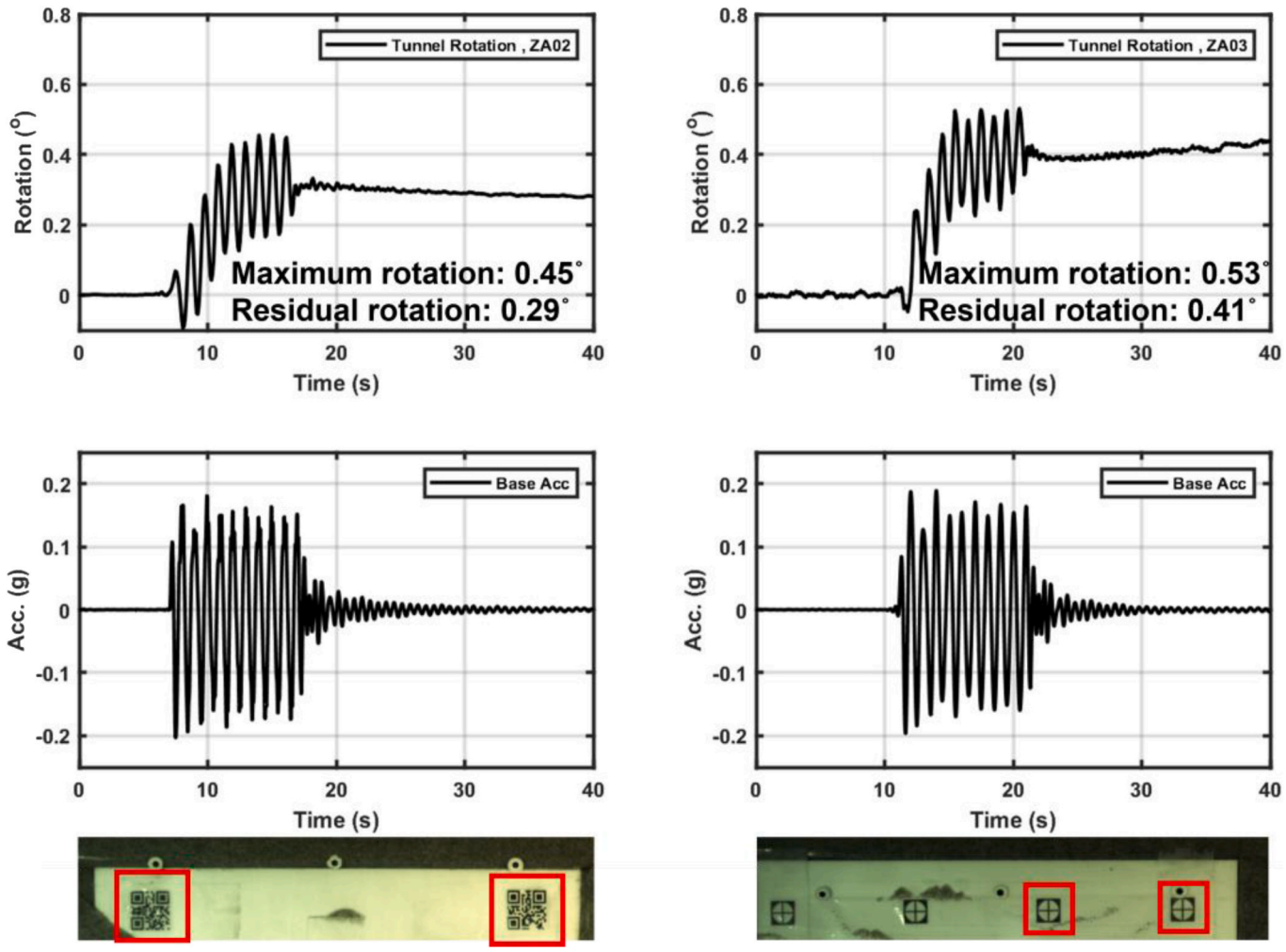

Fig. 16. Tunnel rotation subjected to the input motion (clockwise as positive).

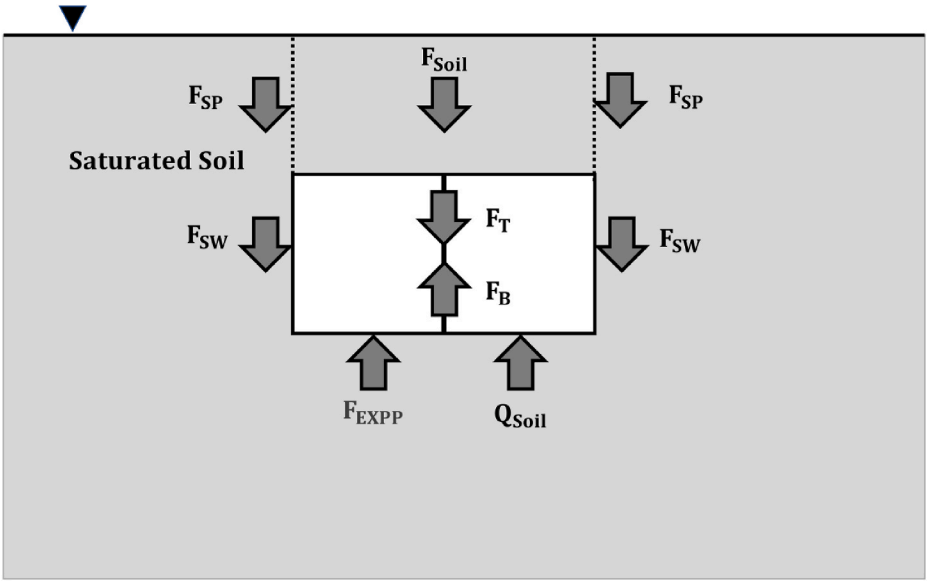

Fig. 17. Force components acting on a rectangular tunnel in liquefied soil.

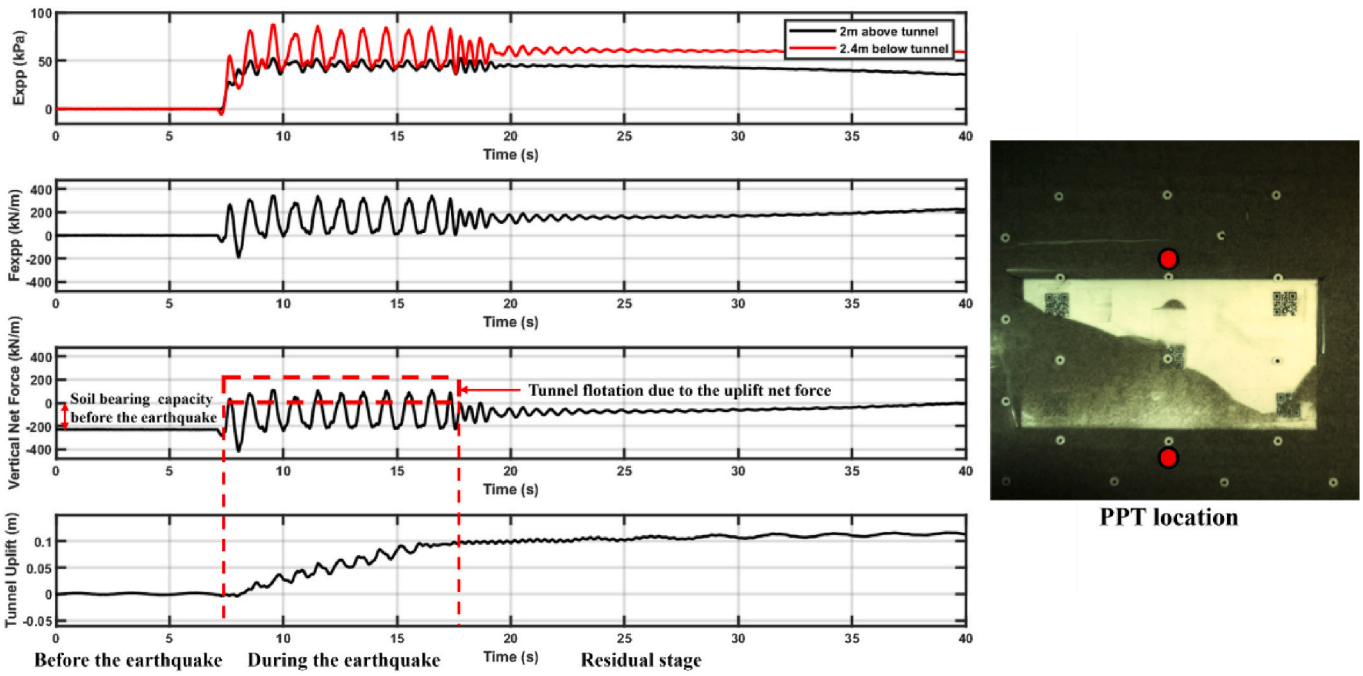

Fig. 18. Tunnel net force and floatation, test ZA02_EQ3 (Prototype scale, positive as upward).

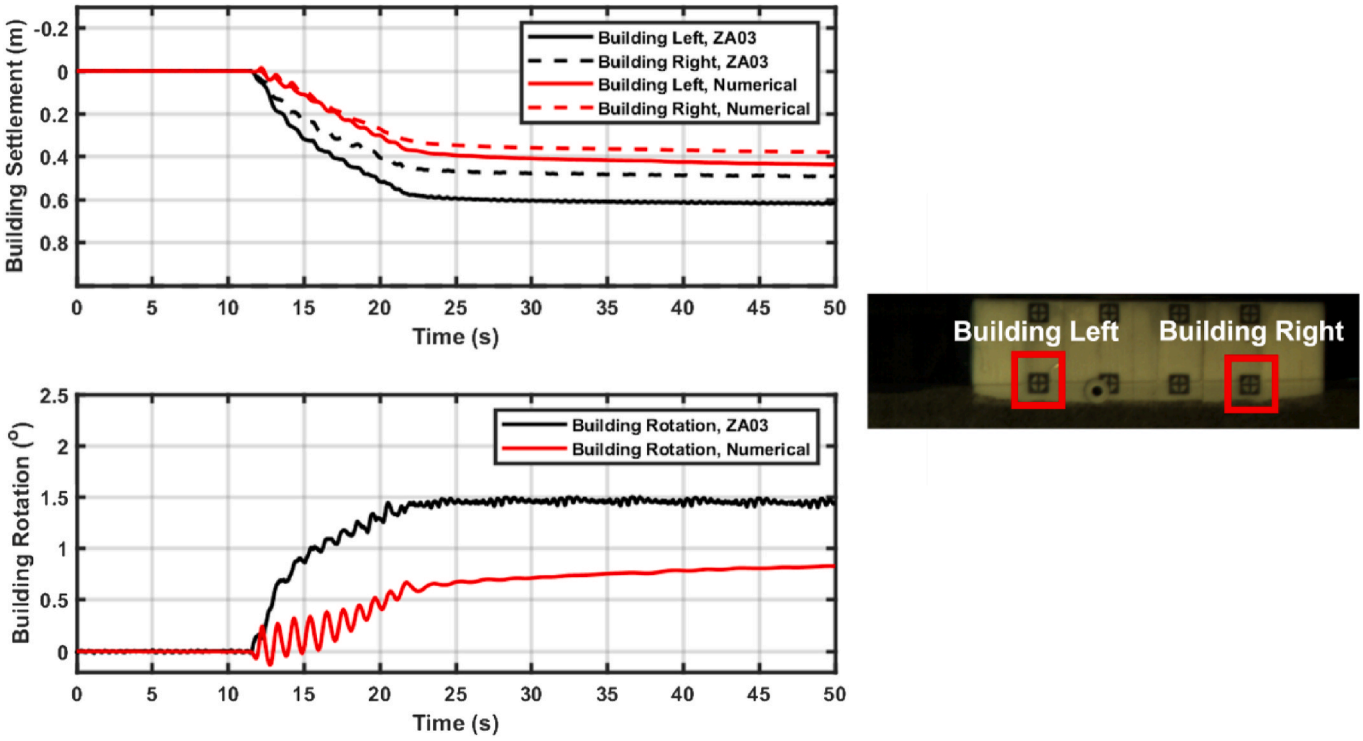

Fig. 19. Building settlement and rotation, test ZA03_EQ2 (Prototype scale, anti-clockwise as positive).

Table 5
Estimated settlements from evaluation methods in comparison to centrifuge test results (Prototype scale)

	Tokimastsu and Seed [51]	Ishihara and Yoshimine [48]	Liu and Dobry [49]	Adamidis and Madabhushi [50] – test OA04	Building settlement (expt.) (left/right) – test ZA03	Building settlement (num.) (left/right) – test ZA03
Building Settlement (m)	0.47	0.81	1.37–6.06	0.46	0.62/0.5	0.44/0.38

presented in Adamidis and Madabhushi [50].

The method of Tokimatsu and Seed [51] estimated the total volumetric strain of about 2.6 % for test ZA03 with relative density of 40 % and maximum shear strain of 12 % beneath the building. The method underestimated the actual settlement of the structure. Estimation from Ishihara and Yoshimine [48] gives a further higher volumetric strain of around 4.5 % with the same input parameters. Boundaries suggest by Liu and Dobry [49] become completely unadoptable for the building with low B/D_L ratio. The effect of the nearby buried shallow tunnel to the adjacent building mainly caused the non-uniform distribution of the building settlement, leading to the rotation of the building. Tunnel effect to the maximum building settlement is not clear by comparing the building settlement reported in test OA04 from Adamidis and Madabhushi [50]. The numerical analyses conducted in this research under-predicted both the building settlement and rotation in the presence of the tunnel, as seen in Fig. 19.

6. Conclusion

Considering the interaction between the surface and sub-surface structures is necessary for a good understanding the dynamic tunnel behaviour. In this study, a set of dynamic centrifuge tests and numerical simulations are conducted to investigate the dynamic structural and soil response subjected to the earthquake loading. The influence of the nearby surface building and tunnel buried depth on the tunnel floatation and soil excess pore pressure generation are studied.

The soil acceleration along various depths attenuated significantly after the first 2 cycles of shaking due to the occurrence of liquefaction. The tunnel floatation following the degradation of soil stiffness is a key seismic design consideration, in particular for shallow underground tunnels constructed using cur-and-cover method in saturated soil. The existence of building surcharge mitigates the soil liquefaction in subsurface within the interaction zone between the tunnel and foundation. More tunnel lateral movement occurred due to the increase of the lateral earth pressure introduced by the building surcharge. This highlights the importance of considering a variety of surface structures and their interactions with tunnels.

Tunnel vertical force mechanism is investigated during the input motion. Vertical net force oscillated during the earthquake due to the variation of the excess pore pressure time histories along the tunnel lining. Building settlements during the earthquake are compared with multiple empirical and analytical estimations as well as numerical analyses. The comparison highlights the importance of the nearby buried tunnel on the non-uniform settlement and consequent rotation of foundations. Furthermore, the presence of the nearby building also increases the tunnel rotation during and after the earthquake.

This research only studies the seismic dynamic tunnel-building interaction based on the certain tunnel-building distance and buried depth of the tunnel with a limited number of centrifuge tests. More physical testing and numerical analyses are required to further understand the effect of tunnel buried depth and relative tunnel-building distance on the mechanism of the dynamic tunnel-building interaction. An experimental campaign in this direction is currently underway.

CRediT authorship contribution statement

Zhengyao He: Data curation, Methodology, Visualization, Writing – original draft. **Gopal S.P. Madabhushi:** Conceptualization, Supervision, Validation, Writing – review & editing.

Declaration of competing interest

The authors declare that they have no known competing financial interests or personal relationships that could have appeared to influence the work reported in this paper.

Data availability

Data will be made available on request.

References

[1] Iida H, Hiroto T, Yoshida N, Iwafuji M. Damage to Daikai subway station. Soils Found 1996;36(Special):283–300.
[2] Yu H, Chen J, Bobet A, Yuan Y. Damage observation and assessment of the Longxi tunnel during the Wenchuan earthquake. Tunn Undergr Space Technol 2016;54:102–16.
[3] Johnson T. Infrastructure damage highlights severe impact of Turkey and Syria earthquakes. N Civ Eng 2023. https://www.newcivilengineer.com/latest/infrastructure-damage-highlights-severe-impact-of-turkey-and-syria-earthquakes-13-02-2023/.
[4] Hashash YM, Hook JJ, Schmidt B, John I, Yao C. Seismic design and analysis of underground structures. Tunn Undergr Space Technol 2001;16(4):247–93.
[5] Tsinidis G, de Silva F, Anastasopoulos I, Bilotta E, Bobet A, Hashash YM, Fuentes R. Seismic behaviour of tunnels: from experiments to analysis. Tunn Undergr Space Technol 2020;99:103334.
[6] Cilingir U, Madabhushi SG. Effect of depth on the seismic response of square tunnels. Soils Found 2011;51(3):449–57.
[7] Cilingir U, Madabhushi SG. A model study on the effects of input motion on the seismic behaviour of tunnels. Soil Dynam Earthq Eng 2011;31(3):452–62.
[8] Cilingir U, Madabhushi SG. Effect of depth on seismic response of circular tunnels. Can Geotech J 2011;48(1):117–27.
[9] Dashti S, Bray JD, Pestana JM, Riemer M, Wilson D. Centrifuge testing to evaluate and mitigate liquefaction-induced building settlement mechanisms. Journal of geotechnical and geoenvironmental engineering 2010;136(7):918–29.
[10] Dashti S, Bray JD, Pestana JM, Riemer M, Wilson D. Mechanisms of seismically induced settlement of buildings with shallow foundations on liquefiable soil. Journal of geotechnical and geoenvironmental engineering 2010;136(1):151–64.
[11] Dashti S, Hashash YMA, Gillis K, Musgrove M, Walker M. Development of dynamic centrifuge models of underground structures near tall buildings. Soil Dynam Earthq Eng 2016;86:89–105.
[12] Hashash YM, Dashti S, Musgrove M, Gillis K, Walker M, Ellison K, Basarah YI. Influence of tall buildings on seismic response of shallow underground structures. J Geotech Geoenviron Eng 2018;144(12):04018097.
[13] Bilotta E, Paolillo A, Russo G, Aversa S. Displacements induced by tunnelling under a historical building. Tunn Undergr Space Technol 2017;61:221–32.
[14] Miranda G, Nappa V, Bilotta E, Haigh SK, Madabhushi GS. Physical modelling of the interaction between a tunnel and a building in a liquefying ground and its mitigation. Tunn Undergr Space Technol 2023;137:105108.
[15] Chian SC, Madabhushi SPG. Effect of buried depth and diameter on uplift of underground structures in liquefied soils. Soil Dynam Earthq Eng 2012;41:181–90.
[16] Watanabe K, Sawada R, Koseki J. Uplift mechanism of open-cut tunnel in liquefied ground and simplified method to evaluate the stability against uplifting. Soils Found 2016;56(3):412–26.
[17] Taylor EJ, Madabhushi SPG. Remediation of liquefaction-induced floatation of non-circular tunnels. Tunn Undergr Space Technol 2020;98:103301.
[18] Madabhushi SSC, Madabhushi SPG. Finite element analysis of floatation of rectangular tunnels following earthquake induced liquefaction. Indian Geotech J 2015;45(3):233–42.
[19] Chian SC, Tokimatsu K, Madabhushi SPG. Soil liquefaction–induced uplift of underground structures: physical and numerical modeling. J Geotech Geoenviron Eng 2014;140(10):04014057.
[20] Chou JC, Kutter BL, Travasarou T, Chacko JM. Centrifuge modeling of seismically induced uplift for the BART transbay tube. J Geotech Geoenviron Eng 2011;137(8):754–65.
[21] Chou JC, Kutter B, Travasarou T. Centrifuge testing of the seismic performance of a submerged cut-and-cover tunnel in liquefiable soil centrifuge data report for test series JCC01. Network for Earthquake Engineering Simulation (NEES) Program, Center of Geotechnical Modeling, Univ. of California, Davis, CA 2008.
[22] Chou JC, Kutter B, Travasarou T. Centrifuge testing of the seismic performance of a submerged cut-and-cover tunnel in liquefiable soil centrifuge data report for test series JCC02. Network for Earthquake Engineering Simulation (NEES) Program, Center of Geotechnical Modeling, Univ. of California, Davis, CA 2008.
[23] Adalier K, Abdoun T, Dobry R, Phillips R, Yang D, Naesgaard E. Centrifuge modelling for seismic retrofit design of an immersed tube tunnel. Int J Phys Model Geotech 2003;3(2):23–35.
[24] Yang D, Naesgaard E, Byrne PM, Adalier K, Abdoun T. Numerical model verification and calibration of George Massey Tunnel using centrifuge models. Can Geotech J 2004;41(5):921–42.
[25] Schofield AN. Cambridge geotechnical centrifuge operations. Geotechnique 1980;30(3):227–68.
[26] Madabhushi G. Centrifuge modelling for civil engineers. CRC press; 2014.
[27] Iai S, Tobita T, Nakahara T. Generalised scaling relations for dynamic centrifuge tests. Geotechnique 2005;55(5):355–62.
[28] Haigh SK, Eadington J, Madabhushi SPG. Permeability and stiffness of sands at very low effective stresses. Geotechnique 2012;62(1):69–75.
[29] Mitrani H. Liquefaction remediation techniques for existing buildings. PhD thesis. Cambridge, UK: University of Cambridge; 2006.
[30] Madabhushi SPG, Houghton NE, Haigh SK. A new automatic sand pourer for model preparation at University of Cambridge. In: Proceedings of the 6th international

conference on physical modelling in Geotechnics. London, UK: Taylor & Francis Group; 2006. p. 217–22.
[31] Madabhushi GS, Haigh SK, Houghton NE, Gould E. Development of a servo-hydraulic earthquake actuator for the Cambridge Turner beam centrifuge. Int J Phys Model Geotech 2012;12(2):77–88.
[32] Steedman RS, Madabhushi SPG. Wave propagation in sands. In: Proceedings of the international conference on seismic zonation. California: Stanford University; 1991.
[33] Ng CWW, Springman SM. Uplift resistance of buried pipelines in granular materials. International conference centrifuge 1994;94:753–8.
[34] Schaminee PEL, Zorn NF, Schotman GJM. Soil response for pipeline upheaval buckling analyses: full-scale laboratory tests and modelling. In: Offshore Technology conference. OnePetro; 1990.
[35] White DJ, Cheuk CY, Bolton MD. The uplift resistance of pipes and plate anchors buried in sand. Geotechnique 2008;58(10):771–9.
[36] Stanier SA, Blaber J, Take WA, White DJ. Improved image-based deformation measurement for geotechnical applications. Can Geotech J 2016;53(5):727–39.
[37] Chan AHC. A unified finite element solution to static and dynamic problems of geomechanics. Doctoral dissertation. Swansea University; 1988.
[38] Madabhushi SPG, Zeng X. Seismic response of gravity quay walls. II: numerical modeling. Journal of geotechnical and geoenvironmental engineering 1998;124 (5):418–27.
[39] Haigh SK, Ghosh B, Madabhushi SP. Importance of time step discretisation for nonlinear dynamic finite element analysis. Can Geotech J 2005;42(3):957–63.
[40] Paston M, Zienkiewicz OC, Leung KH. Simple model for transient soil loading in earthquake analysis. II. Non-associative models for sands. Intl J for Num & Analytical Methods in Geomechanic 1985;9(5).
[41] Zienkiewicz OC, Chan AHC, Pastor M, Schrefler BA, Shiomi T. Computational geomechanics with special reference to earthquake engineering. New York: John Wiley & Sons; 1998.
[42] Madabhushi SS, Haigh SK, Madabhushi GS. LEAP-GWU-2015: centrifuge and numerical modelling of slope liquefaction at the University of Cambridge. Soil Dynam Earthq Eng 2018;113:671–81.
[43] Dafalias YF, Manzari MT. Simple plasticity sand model accounting for fabric change effects. J Eng Mech 2004;130(6):622–34. https://doi.org/10.1061/(asce)0733-9399(2004)130:6(622).
[44] Boulanger RW, Ziotopoulou K. Formulation of a sand plasticity plane-strain model for earthquake engineering applications. Soil Dynam Earthq Eng 2013;53:254–67. https://doi.org/10.1016/j.soildyn.2013.07.006.
[45] Terzaghi K. Theoretical soil mechanics. New York: johnwiley & sons; 1943. p. 11–5.
[46] Seed HB, Lee KL. Liquefaction of saturated sands during cyclic loading. J Soil Mech Found Div 1966;92(6):105–34.
[47] Dashti S, Bray JD. Numerical simulation of building response on liquefiable sand. J Geotech Geoenviron Eng 2013;139(8):1235–49.
[48] Ishihara K, Yoshimine M. Evaluation of settlements in sand deposits following liquefaction during earthquakes. Soils Found 1992;32(1):173–88.
[49] Liu L, Dobry R. Seismic response of shallow foundation on liquefiable sand. Journal of geotechnical and geoenvironmental engineering 1997;123(6):557–67.
[50] Adamidis O, Madabhushi SP. Deformation mechanisms under shallow foundations on liquefiable layers of varying thickness. Geotechnique 2018;68(7):602–13.
[51] Tokimatsu K, Seed HB. Evaluation of settlements in sands due to earthquake shaking. Journal of geotechnical engineering 1987;113(8):861–78.